

IL NUOVO CIMENTO  
DOI 10.1393/ncc/i2005-10213-3

VOL. 29 C, N. 4

Luglio-Agosto 2006

## Novel geometrical concept of a high-performance brain PET scanner. Principle, design and performance estimates

J. SÉGUINOT<sup>(1)</sup>, A. BRAEM<sup>(2)</sup>, E. CHESI<sup>(2)</sup>, C. JORAM<sup>(2)</sup>(\*), S. MATHOT<sup>(2)</sup>,  
P. WEILHAMMER<sup>(2)</sup>, M. CHAMIZO LLATAS<sup>(3)</sup>, J. G. CORREIA<sup>(4)</sup>,  
M. RIBEIRO DA SILVA<sup>(5)</sup>, F. GARIBALDI<sup>(6)</sup>, R. DE LEO<sup>(7)</sup>, E. NAPPI<sup>(7)</sup>,  
F. CORSI<sup>(8)</sup>, A. DRAGONE<sup>(8)</sup>, F. SCHOENAUHL<sup>(9)</sup> and H. ZAIDI<sup>(9)</sup>

<sup>(1)</sup> *Collège de France - Paris, France*

<sup>(2)</sup> *CERN, PH Department - Geneva, Switzerland*

<sup>(3)</sup> *Department of Corpuscular and Nuclear Physics, University of Geneva  
Geneva, Switzerland*

<sup>(4)</sup> *Instituto Tecnológico e Nuclear - Sacavém, Portugal*

<sup>(5)</sup> *Centro de Física Nuclear da Universidade de Lisboa - Lisboa, Portugal*

<sup>(6)</sup> *Istituto Superiore di Sanità - Rome, Italy*

<sup>(7)</sup> *INFN, Sezione di Bari - Bari, Italy*

<sup>(8)</sup> *DEE, Politecnico di Bari - Bari, Italy*

<sup>(9)</sup> *Division of Nuclear Medicine, Geneva University Hospital - Geneva, Switzerland*

(ricevuto il 19 Dicembre 2005; revisionato il 13 Marzo 2006; approvato il 28 Marzo 2006; pubblicato online il 17 Luglio 2006)

**Summary.** — We present the principle, a possible implementation and performance estimates of a novel geometrical concept for a high-resolution positron emission tomograph. The concept, which can be for example implemented in a brain PET device, promises to lead to an essentially parallax-free 3D image reconstruction with excellent spatial resolution and contrast, uniform over the complete field of view. The key components are matrices of long axially oriented scintillator crystals which are read out at both extremities by segmented Hybrid Photon Detectors. We discuss the relevant design considerations for a 3D axial PET camera module, motivate parameter and material choices, and estimate its performance in terms of spatial and energy resolution. We support these estimates by Monte Carlo simulations and in some cases by first experimental results. From the performance of a camera module, we extrapolate to the reconstruction resolution of a 3D axial PET scanner in a semi-analytical way and compare it to an existing state-of-the art brain PET device. We finally describe a dedicated data acquisition system, capable to fully exploit the advantages of the proposed concept.

---

(\*) E-mail: [Christian.Joram@cern.ch](mailto:Christian.Joram@cern.ch)

We conclude that the proposed 3D axial concept and the discussed implementation is a competitive approach for high-resolution brain PET. Excellent energy resolution and Compton enhanced sensitivity are expected to lead to high-quality reconstruction and reduced scanning times.

PACS 87.57.-s – Medical imaging: general.

PACS 87.58.Fg – Positron emission tomography (PET).

PACS 87.61.Ff – Instrumentation.

PACS 29.40.Mc – Scintillation detectors.

## 1. – Introduction

We propose a novel geometrical concept<sup>(1)</sup> of a positron emission tomograph (PET) which aims at an optimized performance in terms of sensitivity, spatial resolution and image contrast. The goal is to maximize the detection efficiency for annihilation photons and, at the same time, to push the spatial resolution towards the physical limits inherent to the annihilation process. Those are determined by the positron range in the organic tissue and the non-collinearity of the 511 keV annihilation photons. A further goal is to achieve an optimized ratio of signal to noise, which finally translates into image contrast.

Our proposal is motivated by the demand of the medical imaging community, expecting comprehensive and high-quality information for a more precise and certain assessment of malign tumours or major neurodegenerative diseases, combined with an improved comfort for the patient during the examination. This implies a significant shortening of the scanning time, or in some cases a reduced injected radiotracer dose.

PET is widely recognized as the best available molecular non-invasive diagnosis technique sensitive to tracer concentrations on the picomole level [1-5]. It provides access to metabolic and kinetic parameters of a particular molecular process and hence not only allows the detection of major diseases but also the follow-up of their treatment.

In recent years there has been significant progress in PET instrumentation, data quantification and image reconstruction [6-8]. PET instrumentation is benefitting of the ongoing development of new particle physics detector components like inorganic scintillators of high density, atomic number and light yield as well as photodetectors like MAPMT, APD and HPD<sup>(2)</sup>. A similar impact has come through advances in microelectronics, which led to highly integrated CMOS front-end circuits, fast data acquisition processors and ultra rapid FPGAs (Field Programmable Gate Arrays).

## 2. – State-of-the-art brain PET instrumentation

One of the most recent and powerful experimental PET devices [9,10] is the so-called High Resolution Research Tomograph (ECAT-HRRT) [11-13], developed by CPS Innovations (Knoxville, TN, USA), which we consider as reference for the new generation of

---

<sup>(1)</sup> Patent application filed under PCT/EP02/07967, international publication number WO 2004/008177 A1.

<sup>(2)</sup> MAPMT = Multi Anode Photomultiplier Tube, APD = Avalanche Photodiode, HPD = Hybrid Photon Detector.

PET scanners. Its performance approaches the physical limits which are intrinsic to a design concept based on the radial arrangement of scintillators blocks, read out with PMTs. The centroid method (Anger logic) and the phoswich technique are used to reconstruct the interaction point of the annihilation photons in the crystal [14]. The ECAT-HRRT consists of octagonal arrangements (42.4 cm face-to-face) of phoswich scintillator block detectors, made of two layers of 64 small LSO crystals (each  $2.1 \times 2.1 \times 7.5 \text{ mm}^3$ ) with 2 different decay times ( $\Delta\tau \approx 7 \text{ ns}$ ). The total active depth is therefore 15 mm. The crystals are oriented normal to the octagon sides, hence essentially pointing in radial direction. Each block is readout by an arrangement of 4 standard PMTs (diameter 19.6 mm), which are optically coupled to the block by means of a light guide which spreads the light from the individual crystals over all 4 PMTs. The centroid corresponds to the true interaction point of the annihilation photon, in case of conversion by photoelectric effect, or to the energy averaged mean position of the interaction in case Compton scattering in the detector is involved.

The phoswich technique is able to roughly halve the uncertainty of the depth of interaction (DOI) and hence significantly reduces the parallax error. However, the phoswich approach is still only a compromise between the maximum crystal depth, which can be tolerated for parallax error reasons, and the minimum length which is required to achieve high detection efficiency. Moreover the phoswich approach demands a delicate pulse shape discrimination of the analogue signal delivered by the PMTs in order to identify the hit crystal layer. The readout electronics becomes unavoidably more complex and possibly limits the data acquisition rate.

The centroid method is intrinsically precise, but the granularity of the Anger logic readout remains relatively poor. It is therefore impossible to track annihilation photons which undergo one or two Compton scatterings in the same detector block. They cannot be rejected as Compton events if the total deposited energy falls inside the energy acceptance window, and hence degrade the spatial resolution. In the case of the HRRT, about 40% of all events fall in this category. A large fraction of these Compton events create energy deposition in both phoswich layers and can in principle be rejected by a careful pulse shape and energy discrimination.

We conclude that a substantial improvement of the PET imaging technique requires a different concept which is able to increase at the same time sensitivity, spatial resolution and background discrimination. The ultimate performance requires a thick and finely segmented array of high-density and high- $Z$  scintillating crystals, *individually* read out. Precise 3D reconstruction of the photon interactions in such a crystal matrix allows to track annihilation photons which undergo photoelectric or Compton scattering. Compton events, if unambiguously reconstructed, are able to enhance the sensitivity without degrading image quality or contrast. Finally it is the patient who profits from this in form of a lower injected radioactive dose or a reduced scanning time which not only improves the patient's comfort but also lowers the risk of patient movements during the scan.

Co-registration of the metabolic activity by PET with a precise imaging of the anatomic structure using either X-ray computed tomography (CT) or magnetic resonance imaging (MRI) is a proven way of improving the diagnostic potential. This multimodality approach allows, by means of image fusion, for an accurate localisation of the detected radiotracer emission pattern. In addition the CT/MRI information can be used to correct for photon attenuation in the tissue, an effect which still leads to false estimation of the source intensity and hence prevents a precise quantification of PET data [15].

Several developments projects in PET instrumentation have been proposed or are currently under design or test. To our knowledge, most of them rely on the classical radial scintillator arrangement.

In this paper we describe in detail a concept for a brain PET scanner based on long scintillating crystals which are axially oriented. This concept allows to achieve the maximum detection efficiency and at the same time provides precise 3D and parallax free reconstruction of photoelectric and Compton events over the full field of view (FOV). The spatial resolution in the transaxial plane does not depend on the source position and matches the intrinsic physical limitations due to the range of the positron in the organic tissue and the non-collinearity of the 511 keV annihilation photon pair.

The axial arrangement of the scintillating crystals is a natural and straightforward idea to suppress the parallax error which is inherent to all radial geometries. As we discovered only recently, essential parts of the concept described in this paper, were already proposed in 1988 [16], however the proposal seemed pre-mature given the state-of-the-art of scintillating crystals and photodetectors at that time. Matrices of BGO crystals ( $3 \times 5 \text{ mm}^2$ ) of 50 mm length were intended to be read out on both ends by position sensitive PM tubes with crossed wire anodes. Such a readout does not permit to track photon interactions in the crystal matrix and therefore leads to reconstruction ambiguities for Compton interactions. In addition the modest light yield of BGO crystals compromised the achievable reconstruction resolution in the axial direction. The authors have not pursued this development much further, which probably also explains why it is not mentioned in recent appropriate review articles [1-4].

The paper is organized as follows: In sect. 3 we describe the geometrical concept of a 3D axial PET camera and its principle of operation. We discuss the key components, *i.e.* the long scintillators and the segmented Hybrid Photon Detectors. Section 4 is devoted to performance estimates in terms of spatial and energy resolution, based on analytical and Monte Carlo calculations. We also derive an estimate of the achievable image reconstruction resolution and compare it with the HRRT as an existing state-of-the-art device. It is followed by a detailed discussion of the achievable sensitivity and its enhancement by exploiting events which involve Compton scattering in the crystal matrix (sect. 5). In sect. 6 we define a specific factor of merit, allowing an overall characterisation and benchmarking of the concept and its implementation. We finally (sect. 7) present a conceptual study of a dedicated data acquisition system, which is able to exploit the advantages of the 3D axial concept and its segmented photon detectors.

### 3. – The 3D axial geometry with HPD readout—A novel concept

In the following we describe in detail the principle and a possible implementation of a 3D axial PET concept using HPDs for the readout of the scintillation light. The basic features of the concept have already been described briefly in previous publications [17-19].

**3.1. Geometry and principle of operation.** – We propose detector modules which, for a brain PET scanner (fig. 1), could be arranged in a ring<sup>(3)</sup> of 35 cm inner free diameter. The distance between opposite crystals is in this case about 38 cm.

A detector module (fig. 2) consists of an array of long (15 to 25 cm depending on the

---

<sup>(3)</sup> A second concentric ring with larger diameter can be added for full azimuthal coverage.

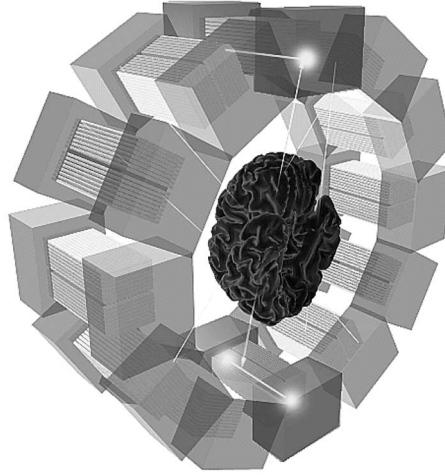


Fig. 1. – Schematic representation of a PET scanner based on 3D axial detector modules.

scintillating material) optically polished crystals of small cross-section ( $3.2 \times 3.2 \text{ mm}^2$ ), axially oriented and separated by 0.8 mm. Each array of  $16 \times 13$  crystal bars is optically coupled at both ends to proximity focused Hybrid Photon Detectors made with a thin sapphire entrance window and a bi-alkali photocathode. The HPDs feature a Si sensor with a readout granularity of  $4 \times 4 \text{ mm}^2$  to accurately match the matrix configuration.

A large fraction of the scintillation light is trapped in the crystal bar and propagates by total internal reflection to the opposite extremities. In the transaxial ( $x, y$ )-plane the highly segmented geometry provides, from the readout of the crystal bar address,

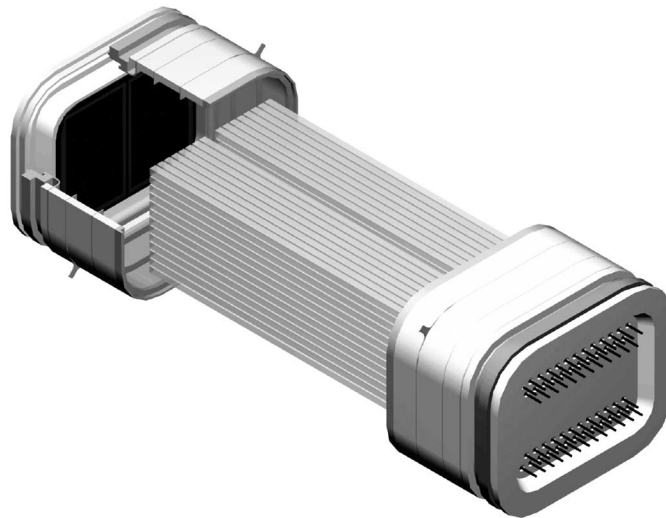


Fig. 2. – Drawing of a 3D axial detector module consisting of a matrix of 150 mm long crystals, read out by two HPDs.

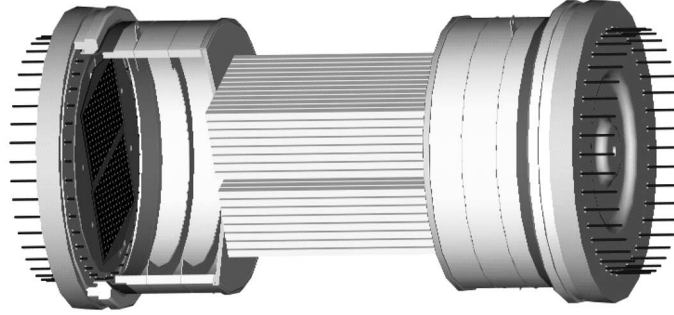


Fig. 3. – Prototype of a 3D axial detector module for proof of principle measurements. The scintillator matrix is composed of already available YAP crystals of dimensions  $3.2 \times 3.2 \times 100 \text{ mm}^3$ .

accurate  $x, y$  coordinates with an excellent and uniform resolution (see sect. 4), totally independent of the detector thickness. The line of response (LOR) reconstructed from a detected 511 keV annihilation photon pair is consequently free of the parallax error intrinsic to the classic radial detector geometry. It results that the detector thickness can be increased up to 3 attenuation lengths which roughly double the sensitivity to photoelectric interactions compared to conventional detectors.

The measurement of the asymmetry of the amounts of light detected at the two crystal ends provides, with good accuracy, the determination of the axial coordinate  $z$  (see subsect. 4.3). The total deposited photon energy can be derived with good precision from the sum of the signals at the two ends, as the light attenuation during the propagation through the crystals can be corrected for.

The fine segmentation in the transaxial plane allows the tracking of single or multiple Compton scatterings in the matrix. Their reconstruction, with a measurement of the total energy lost provides, unambiguously, an enhancement of the detection efficiency of 511 keV photons (sect. 5).

As the critical angle for reflection at the interface with the sapphire window is higher than the maximum incident angle for LSO or  $\text{LaBr}_3$  crystals, the number of photons transmitted onto the photocathode is only determined by the fraction of light trapped inside the bar and its attenuation in the crystal bulk. Because of the good match of the refractive indices at the wavelength of the scintillation light <sup>(4)</sup>, the loss of photons by reflectivity at the interface crystalwindow is negligible.

The robustness of sapphire permits the use of a very thin (1.8 mm) window in order to limit the light spreading on the adjacent readout channels. Figure 3 is an illustration of a detector module designed for the demonstration of the concept with two round 5-in. HPDs. The gap of 0.8 mm between crystal bars is defined by means of nylon strings stretched at both ends on accurate frames without screening between bars to absorb the refracted light coming out of the crystal at the scintillation emission point.

**3.2. The scintillator matrix: Fast Ce-doped inorganic crystals.** – Table I summarizes the physical properties of Cerium-doped inorganic fast scintillators already available, or

---

<sup>(4)</sup>  $n_{\text{sapphire}} = 1.798$  at 350 nm for  $\text{LaBr}_3$  ( $n = 1.88$ );  $n_{\text{sapphire}} = 1.780$  at 420 nm for LSO ( $n = 1.82$ ).

TABLE I. – *Properties of scintillation crystals used for PET.*

Scintillator	BGO <sup>(1)</sup>	LSO <sup>(2)</sup>	LYSO <sup>(3)</sup>	GSO <sup>(4)</sup>	LuAP <sup>(5)</sup>	LaBr <sup>(6)</sup>	YAP <sup>(7)</sup>
Density (g/cc)	7.1	7.4	7.1	6.7	8.3	5.3	5.4
Light yield (photons/keV)	9	27	32	8	10	61	21
Effective $Z$	75	66	64 <sup>(*)</sup>	60	65	46.9	31.4
Principal decay time (ns)	300	42	48	30-60	18	35	25
Peak wavelength (nm)	480	420	420	440	365	358	370
Index of refraction	2.15	1.82	$\approx 1.8$	1.95	1.95	1.88	1.94
Photofraction at 511 keV(%)	41.5	32.5	34.4 <sup>(**)</sup>	25	30.6	15	4.5
Attenuation length at 511 keV(cm)	1.04	1.15	1.12	1.42	1.05	2.13	2.19
Energy resolution <sup>(***)</sup> at 662 keV (%)	7.9	8	7.1	6.9	10	2.9	3.8
Hygroscopic	No	No	No	No	No	Yes	No

<sup>(1)</sup> Bi<sub>4</sub>Ge<sub>3</sub>O<sub>12</sub>; <sup>(2)</sup> Lu<sub>2</sub>SiO<sub>5</sub>:Ce; <sup>(3)</sup> LuYSiO<sub>5</sub>:Ce; <sup>(4)</sup> Gd<sub>2</sub>SiO<sub>5</sub>:Ce; <sup>(5)</sup> LuAlO<sub>3</sub>:Ce; <sup>(6)</sup> LaBr<sub>3</sub>:Ce; <sup>(7)</sup> YAlO<sub>3</sub>:Ce

<sup>(\*)</sup> Calculated; <sup>(\*\*)</sup> Result of simulation with Geant4; <sup>(\*\*\*)</sup>  $\Delta E/E$  FWHM.

still under development, which can be considered for an advanced PET system [20-30].

On the medium term, Cerium doped Lutetium Oxiorthosilicate (LSO: Ce) (CTI Molecular Imaging, Knoxville, TN, USA), Lutetium Yttrium Oxyorthosilicate (LYSO:Ce)<sup>(5)</sup> and Lanthanum Bromide (LaBr<sub>3</sub>:Ce)<sup>(6)</sup> are the most promising candidates. LSO and LYSO have the significant advantage of a short attenuation length and a high photo fraction at 511 keV compared with LaBr<sub>3</sub>. They are not hygroscopic and can be handled without special precaution contrary to LaBr<sub>3</sub>. However the performance of LSO is much worse than the one of LaBr<sub>3</sub> in terms of light yield, energy resolution and linearity of the response with energy. The peak wavelength of the scintillation light at 358 nm for the LaBr<sub>3</sub>, compared to 420 nm for LSO, leads to a higher detection efficiency due to the blue-enhanced sensitivity characteristics of standard (bi-alkali) photocathodes (see subsubsection. 3.3.2).

The use of long crystal bar (15 to 25 cm) in one or two pieces optically coupled, imposes more constraints for the fabrication (growing, cutting and polishing) and for the mechanical (robustness) and the optical (surface quality) properties. The production of crystals of this length is technically feasible, however it may have an impact on the cost.

The adjustment and the calibration of the light attenuation in the crystal bars is a key parameter since they determine the reconstruction accuracy of the axial coordinate and the energy resolution. These aspects are discussed in sects. 3 and 4 for LSO and LaBr<sub>3</sub> crystals. Recent experimental studies on this subject are reported in [31].

Studies with LYSO samples have revealed promising characteristics. They show an energy resolution comparable to LSO, but, in contrast to LSO, the response scales linearly with energy. Producers claim that a photon yield of  $35 \cdot 10^3$  photons/MeV is attainable (LYSO with  $31 \cdot 10^3$  photons/MeV is already available from St. Gobain). If these performances are confirmed in future, LYSO would be a very good candidate.

Ce doped LuAP [32] crystals can presently not be used because of their low light yield (about  $10^4$  ph/MeV) despite very good physical properties especially their short decay time (18 ns) compared to LSO (42 ns). However new developments<sup>(7)</sup> indicate that a photon yield of  $20 \cdot 10^3$  ph/MeV is possible, opening interesting perspective on a longer time scale.

<sup>(5)</sup> Photonic Materials Ltd, Scotland.

<sup>(6)</sup> Available under the name *BrilLanCe 380* from Saint Gobain Crystals, France.

<sup>(7)</sup> Photonic materials Ltd., Bellshill, Scotland, UK.

### 3'3. The PET HPD—a Hybrid Photon Detector with enclosed VLSI readout electronics.

– HPDs [33-35] are unique photon detectors for medical imaging applications compared to standard PMTs and commercially available APDs. An HPD consists of a vacuum envelope with a transparent entrance window on which a semitransparent photocathode is evaporated. A photoelectron, ejected from the photocathode (on potential  $U_C$ ), is accelerated towards the segmented silicon anode (ground potential), in which, on impact, a large number of electron-hole pairs and hence a detectable signal is produced. The gain of the HPD is  $M \equiv N_{e-h} \approx e \cdot U_C / W_{Si}$  with  $W_{Si} = 3.6$  eV being the energy needed to create an electron-hole pair in silicon.

HPDs combine the sensitivity to single photons, known from standard vacuum phototubes, with the exceptional spatial and energy resolution and the great design flexibility (size and geometry) of silicon sensors. Photon detectors of large sensitive area with a high readout granularity can be fabricated. The multiplexed VLSI front-end readout electronic is encapsulated in the HPD detector body. This minimizes the effective capacitance to a few pF per channel and hence improves the signal characteristics (bandwidth and noise). The number of connecting lines (vacuum feedthroughs) required for the data acquisition is reduced by about a factor of 5 with respect to the number of channels.

APDs [36,37] are the most promising competitors to be compared with HPDs. Commercially available APDs are mostly mono channel photon detector of about 20 mm<sup>2</sup> acceptance. They are insensitive to axial and transversal strong magnetic fields. APD arrays [38-41] of 32 channels (typically  $2 \times 2$  mm<sup>2</sup>/channel) have been developed. The configuration of the scintillator matrix has to be adapted to the available readout granularity, while HPDs can be designed and built to match a crystal array with optimized geometry.

Proximity focused HPDs can be operated in strong magnetic fields, as long as the field direction is aligned with the tube axis. Axial magnetic fields have even the beneficial effect of reducing the so-called point spread function, which is a consequence of the angular and energy distribution of the photoelectrons at emission from the photocathode, and therefore lead to an improved spatical resolution.

The sensitivity of HPDs is determined by the quantum efficiency of the semi transparent bi-alkali photocathode which, at 400 nm, is about 30 to 50% lower than the quantum efficiency of reverse [42] and high-capacitance APDs<sup>(8)</sup>, respectively.

HPDs operated at a moderate acceleration voltage of  $U_C = 12$  kV have a gain of  $M \approx 3 \cdot 10^3$ , well adapted to the performances of modern front-end electronics with an Equivalent Noise Charge ( $ENC$ ) of  $< 2 \cdot 10^3$  electrons. If required, they can be operated up to 20 kV increasing the gain to  $5.5 \cdot 10^3$  without lack of performances. The gain is achieved in a single stage dissipative process and is therefore practically free of avalanche related excess fluctuation. Consequently, the Excess Noise Factor  $ENF$ , which enters in the energy resolution of the detection system (see subsect. 3'2) is only 1.09 compared to  $1.4 \pm 0.05$  for PMTs. The small excess noise of an HPD is caused by those  $\approx 20\%$  of photoelectrons which are back scattered from the silicon sensor and deposit only partially their kinetic energy.

Intrinsic to their principle of operation, the linearity of the response with the incident light (or energy deposition in the crystal) is excellent. Gain and signal characteristics are unaffected by variations of the detector temperature. In principle, APD can achieve gains up to  $10^3$ , but, in practice, their use is limited to gains of few  $10^2$  for an acceptable

---

<sup>(8)</sup> Cf. data sheets of Hamamatsu APDs



stability ( $1/M \times dM/dV = 3.1\%/V$ ) with the operating voltage  $V$ . Moreover their  $ENF$  increases linearly with the gain [43] and usually varies from  $ENF = 2$  or  $3$  for  $M = 50$  to  $ENF = 9$  for  $M = 10^3$ . Therefore, even with a gain of 50, the energy resolution with an APD is 50 to 70% worse compared to a HPD operated at gains of  $3$  to  $5 \times 10^3$ .

The temperature dependence ( $1/M \times dM/dT$ ) of APDs is about  $-2\%/K$  requiring cooling, and their dark current at room temperature is of the order of few nA for  $M = 50$ , instead of few tens of pA/pad for HPDs independently of the gain.

The use of APDs at low gain finally requires very low noise front-end electronics; a challenging development if fast response is required with stray capacitances in the 100 pF range.

A last and important advantage of HPDs is the possibility of reading out the induced signal on the non-segmented Si sensor back plane (the side on which the accelerated photoelectrons hit the sensor) providing a fast measurement of the total energy deposited in the full Si sensor, *i.e.* in the total crystal matrix coupled to the HPD. This unique feature of the HPDs allows for a simple and fast photon energy discrimination—without need to readout the individual detector channels. The back plane information can be used to discriminate annihilation photons which underwent Compton scattering in the organic tissue of the body or in the crystal matrix with incomplete energy deposition. Moreover, the fast back plane signals can be used to find coincident detector modules with a time resolution of potentially 5 ns (see sect. 7).

We believe that HPDs are at the moment the best performing and flexible position sensitive photon detectors for our PET concept. If one wanted to implement it with available state-of-the-art Multi Anode PMTs like the Hamamatsu 8500 or 9500 one would face a number of problems: The segmentation of these devices is either too coarse (6 mm) or too small (3 mm). Windows with high refractive index which are well matched to the crystals' index are not available. The signal amplitudes of the MAPMT are comfortably large, but all channels need to be calibrated separately to cope with channel-to-channel gain variations of up to a factor 3. The above described feature of the fast backplane readout would be very hard to implement in an online way.

A dedicated plant has been designed and built at CERN to produce HPDs up to 10 in diameter, as well as all the various technologies needed to prepare the components [44-48]. The prototype of a proximity focused HPD for PET applications which we describe below has entirely been designed, developed and fabricated in this framework.

**3.3.1. Design of the PET-HPD.** The prototype proximity focused HPD developed at CERN is a round photodetector with a bi-alkali photocathode deposited on a thin (1.8 mm) flat sapphire entrance window of 105 mm diameter (see drawing and photograph in figs. 4 and 5). The total length of the HPD is 67 mm. A cross-section of the HPD is shown in fig. 6 with the electron optical configuration simulated using the SIMION<sup>(9)</sup> code). The window is sealed to a metallic ring made of niobium which assures the connection for the photocathode polarization. A set of two electrodes in niobium (0.7 mm thick) inserted in between cylindrical alumina spacers (ceramic) guarantee a precise 1:1 electron optical image transfer (*i.e.* proximity focusing) from the photocathode onto the silicon sensor. At the base of the body a skirt in kovar is welded to a stainless steel flange equipped with a gold plated sharp edge knife. The ceramic rings, the sapphire window and the metallic components in niobium and kovar are joined by means of active high

---

<sup>(9)</sup> SIMION 3D, Scientific Instruments Services Inc., Ringoes, NJ 08551, USA.

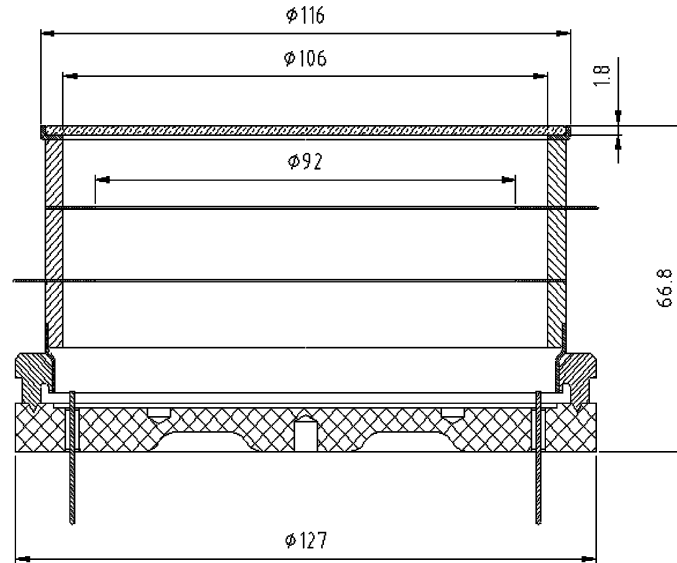


Fig. 4. – Cross-section of the proximity focused prototype HPD.

temperature vacuum brazing. Details on the tube manufacturing and the indium sealing technology which is used to seal the tube in-situ after photocathode processing are given in [45].

The ceramic hybrid carrier which supports the sensor and the readout VATA chips is wire bonded to 40 vacuum feedtroughs of the base plate to provide the control and data lines connections to the data acquisition system.

The sensor consists of a 300 microns thick rectangular silicon plate with  $16 \times 13$  pads implemented as  $p^+n$  junctions, DC coupled to the front end electronic. The 208



Fig. 5. – Photograph of a proximity focused prototype HPD with round silicon sensor and integrated front-end electronics.

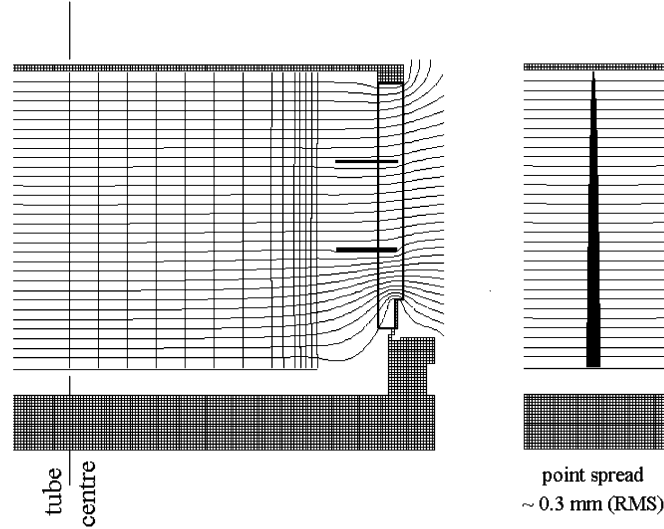


Fig. 6. – Cross-section of the proximity focused HPD as used in SIMION simulations. Left: Equipotentials and individual electron trajectories. Right: Bundle of electron trajectories from a point source allowing to determine the point spread function.

pads of  $3.96 \times 3.96 \text{ mm}^2$  with a gap of 80 microns match precisely the crystal matrix configuration. The pad size is larger than the crystal bar cross-section ( $3.2 \times 3.2 \text{ mm}^2$ ) to cope with the light spread on the photocathode due to the non-zero thickness of the HPD entrance window. This reduces the optical signal sharing with adjacent channels (see subsect. 4.1).

**3.3.2. Performance of the prototype HPD.** The proximity focused prototype HPD shown in fig. 5 has been fabricated with the goal to study its electron optical and electrical properties, but also to validate the complete fabrication procedure. The HPD is equipped with a round 50 mm diameter Si sensor of 2048 pads of  $1 \times 1 \text{ mm}^2$  connected to 16 standard readout VA prime chips. This high granularity Si sensor allows to map out with high precision the electron optical properties. Figure 7 shows the quantum efficiency of the photocathode of this first proximity focused prototype HPD. Once the cathode processing parameters are optimized, we expect a 10–15% higher sensitivity, similar to other HPDs, which we have fabricated.

The window was scanned along diameters with a fine light spot ( $\approx 0.5 \text{ mm RMS}$ ) generated by a self-triggered  $\text{H}_2$  flash lamp. The resulting correlation between the radial position of the light spot and the centre of gravity of the charge distribution measured with the Si sensor exhibits, as shown in fig. 8, a perfect 1:1 linear imaging within 1% deviation. The point spread function which describes the charge distribution for a point source is of the order of 0.3 mm (RMS). Figure 9 shows for a fixed spot position the variation of the total charge measured in the image spot with the acceleration voltage. Above 10 kV, the variation is strictly linear. Below this value, *i.e.* at photoelectron energies below 10 keV, the energy loss in the dead  $\text{n}^+$  layer implanted on the entrance bias side of the wafer increases and favours a minimum operating voltage of 12 kV.

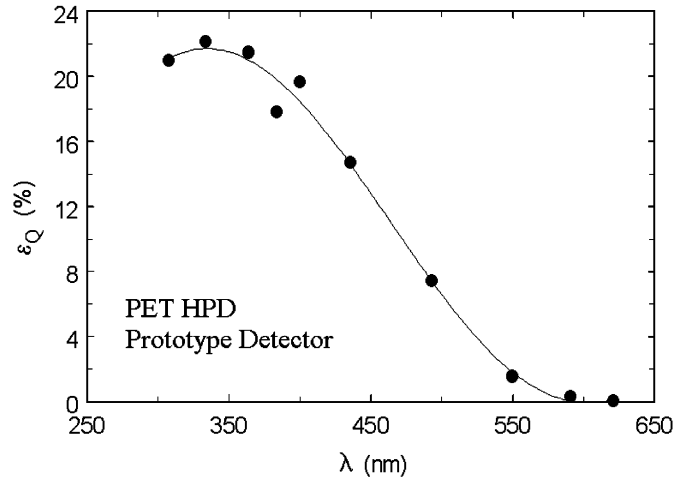


Fig. 7. – Measured quantum efficiency of the first prototype HPD.

**3'4. The VLSI auto-triggering front-end electronic: the VATA-GP5.** – The front-end electronic is an important component of the PET concept designed to cope with high counting rates (up to 2 MHz per module of 208 channels) and to be operated in a self-triggering mode with a sparse readout of the data in order to optimize the data taking rate.

The VATA-GP5 chip is an optimized ASIC version of the existing VATA-GP3 and

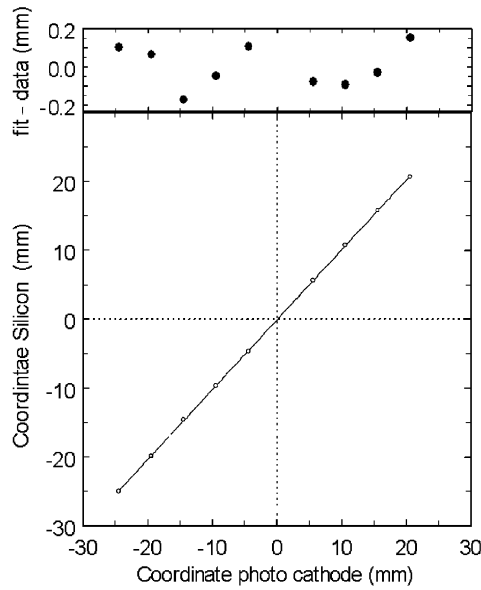


Fig. 8. – Measured relation between the photon coordinate at the photocathode and the photoelectron hit on the silicon sensor.

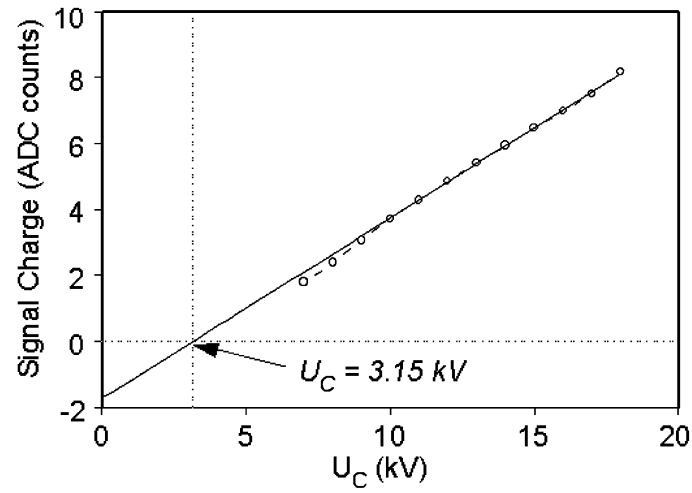


Fig. 9. – Pulse height (a.u.) *vs.* cathode voltage (kV).

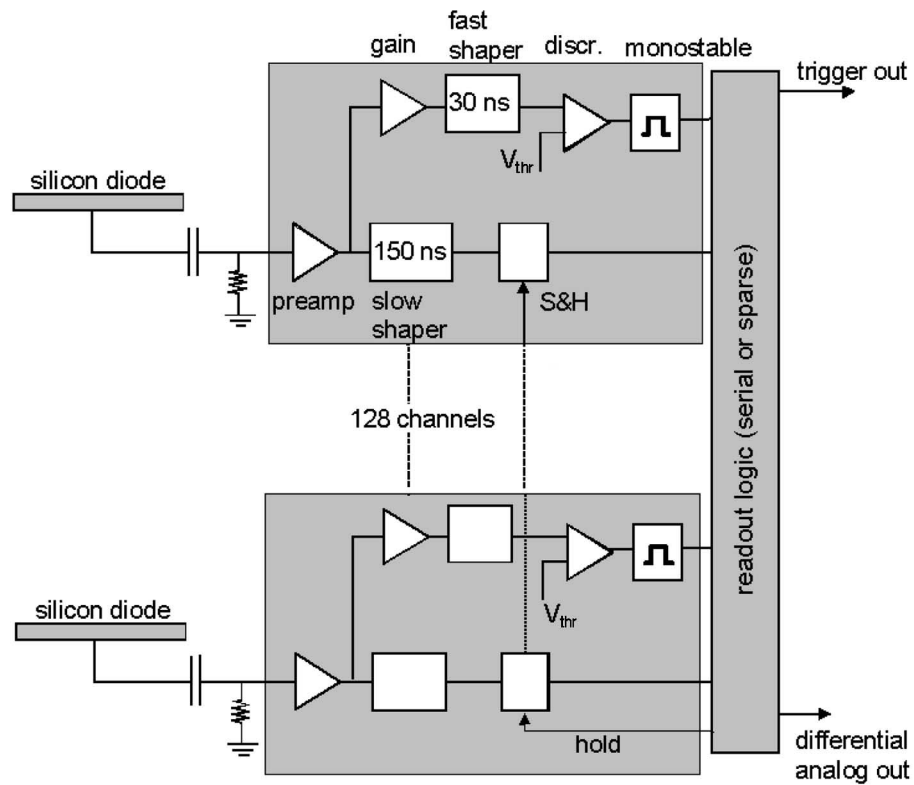


Fig. 10. – Schematic and simplified block diagram of the VATA-GP5 circuit.

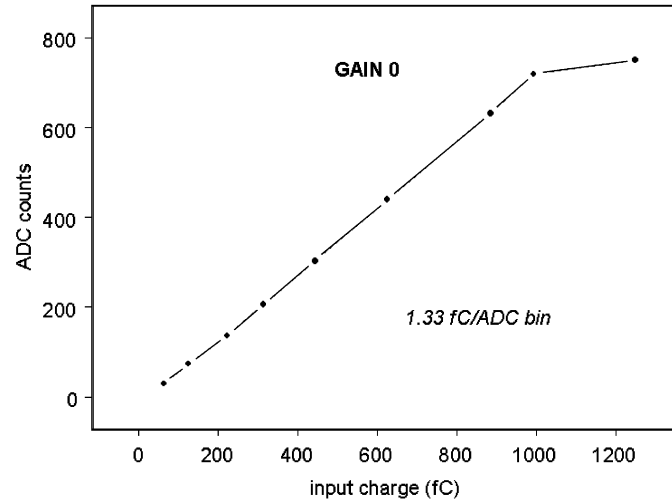


Fig. 11. – Response of the VATA-GP5 amplifier/shaper circuit to injected input charges from 0.06 to 1.25 pC.

was developed for the PAD HPD by IDEAS (Ideas ASA, Norway) in collaboration with CERN. For cost reasons the first prototype version was produced in 0.6 micron CMOS technology in order to validate the PET concept. In the future the chip should be implemented in deep submicron technology to increase the bandwidth and thus lead to optimal performance in terms of response speed, as required by a full PET system.

The VATA chips comprise 128 channels and is equipped with three readout modes: serial, sparse and sparse with adjacent channels.

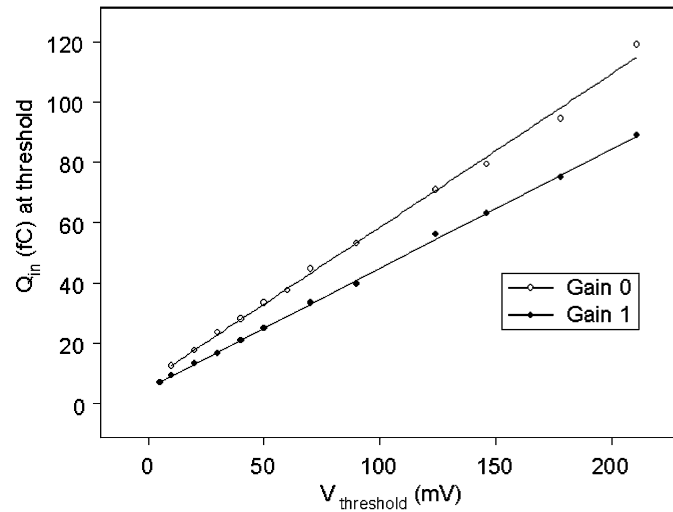


Fig. 12. – Characterization of the VATA-GP5 fast discriminator circuit with injected input charges from 0 to 120 fC.

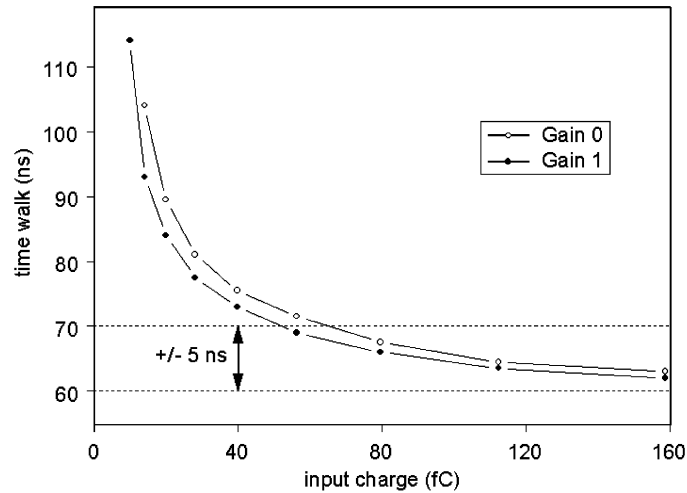


Fig. 13. – Characterization of the VATA-GP5 time walk compensation in the input charge range 10 to 160 fC.

Figure 10 shows a block diagram of the VATA-GP5. The charge amplifier is optimized for a total detector capacitance of 5 to 7 pF and an input dynamic range of 1.2 pC for positive polarity.

The analogue chain is a classical arrangement, where a Sample and Hold (S/H) signal is applied at the peaking time (150 ns) of the “slow” shaper when a coincidence between a pair of modules is detected by an external logic (see sect. 7). The hold signal stores the amplitude proportional to the input charge, to be later readout. The excellent linearity of the amplifier/shaper circuit is demonstrated in fig. 11, where signals in the range from 0.06 to 1.25 pC were injected. Above 1 pC saturation effects become noticeable, which are however due to the limited dynamic range of the ADC. The signal from the “fast” shaper, of 40 ns peaking time, goes to a discriminator. A common threshold is applied to all channels. Individual channels can be trimmed by 4 bit DACs. Figure 12 shows for two gain settings the excellent linearity of the discriminator in the range 0 to 120 fC. A time-walk compensation circuit is implemented at the input of each discriminator to suppress timewalk due to different signal amplitudes. The effect of the time walk compensation is shown in fig. 13. Signals in the range from 60 to 160 fC are compensated within  $\pm 5$  ns. The outputs of all the 128 discriminators are then ORed together providing a Fast Or signal (*FOR*) able to detect coincidences with an expected timing resolution of less than 10 ns. The VATA chip provides in addition a *FOR* signal with an amplitude proportional to the multiplicity of hit channels.

When a discriminator output is activated, the corresponding address of the channel is stored in a register. In sparse readout mode, if a *FOR* is detected, a veto signal blocks the generation of further *ORs* and only the analogue values of the hits channels with their address will be readout.

In normal PET operation the coincidence between two annihilation photons is established externally (see sect. 7) on the basis of the silicon backplane signals. On the contrary, if no coincidence is found, a reset signal is applied to the register in a minimum time delay ( $< 12$  ns) in order to reduce the probability of having accidentals recorded

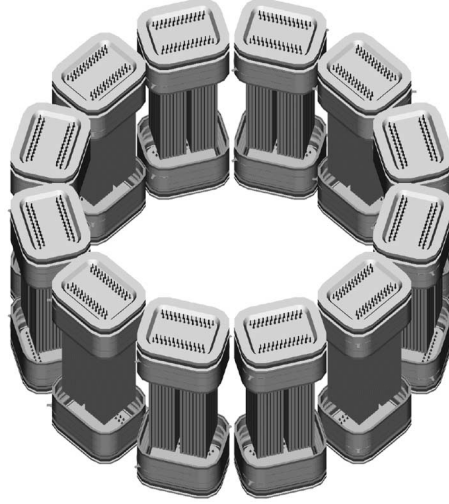


Fig. 14. – Possible arrangement of 3D axial modules to a ring scanner.

when applying the common S/H signal. In addition, each discriminator output can be masked in case of malfunctioning of a channel.

The data acquisition speed is determined by the readout clock frequency which is currently limited to 20 MHz. The readout time is proportional to the number of hit channels plus three clocks per chip which are needed before to reach the first stored data.

If the sparse readout mode is an essential feature to maximize the data acquisition rate, the serial readout is needed to test the correct functioning of all the channels by injecting a calibrated pulse into each input, and register the pedestals for subtraction.

The lowest threshold of the fast discriminator ranges from 4 to 6 fC including the threshold spread after tuning with the channel trim DAC. It corresponds to about 5 sigmas of the shaper noise. With an HPD operated at 12 kV ( $M = 3 \cdot 10^3$ ) a threshold setting of 5 fC would select annihilation photons (or recoil electrons) of energy higher than 10 to 12 keV for a scintillator matrix with LSO crystals. For  $\text{LaBr}_3$  scintillators, the same threshold would provide a factor of about 1/3 on the minimum energy.

The equivalent noise charge ( $ENC$ ) of the slow shaper is of about  $2 \cdot 10^3$  electrons, a negligible contribution to the energy resolution ( $< 0.1\%$ ) at 511 keV.

Results from a recent test of a custom-design PET-HPD tube equipped with a VATA-GP5 readout chip are reported in [49].

**3'5. Configuration of a PET scanner.** – Figure 14 shows a possible arrangement of 12 modules in a ring of 350 mm free inner diameter with rectangular HPDs. Those could be fabricated with a moderate upgrade of the tooling and production facilities. A full azimuthal coverage would require a second concentric ring at larger radius.

#### 4. – Spatial reconstruction and energy determination

In the following we discuss the spatial and energy resolution which can be achieved with the axial concept. We also perform a direct comparison of certain characteristics



between the axial and a conventional radial geometry.

**4.1. Number of detected photoelectrons.** – The number of scintillations photons  $N_{\text{ph}}$  generated by a 511 keV photon is  $13.8 \cdot 10^3$  and  $31.2 \cdot 10^3$  in LSO and LaBr<sub>3</sub>, respectively. Ignoring initially the light absorption in the crystal bulk, the total light trapping and transport efficiency  $\epsilon_{\text{TT}}$  has been determined by means of a microscopic photon transport Monte Carlo code (see below). As the light propagates by total internal reflections, almost perfect reflectivity (99.9% at each bounce) has been assumed. For square crystals of  $3.2 \times 3.2 \text{ mm}^2$ ,  $\epsilon_{\text{TT}}$  has been found to be 0.614 (LSO) and 0.60 (LaBr<sub>3</sub>). The small difference is due to the small difference in refractive index of the two materials.

With  $\epsilon_Q$  being the quantum efficiency of the bi-alkali photocathode at the wavelength of the scintillation peak emission ( $\epsilon_Q = 0.18$  for LSO and 0.25 for LaBr<sub>3</sub>), the total number of photons detected ( $\equiv N_{\text{p.e.}}$ ) at the two ends of the crystal is

$$(1) \quad N_{\text{p.e.}}(z) = N_1(z) + N_2(z) = \frac{N_0}{2} \cdot [e^{-z/\lambda} + e^{-(L_C-z)/\lambda}]$$

with

$$(2) \quad N_0 = N_{\text{ph}} \cdot \epsilon_Q \cdot \epsilon_{\text{TT}} = \begin{cases} 1525 \pm 39 & (\text{LSO}) \\ 4681 \pm 68 & (\text{LaBr}_3) \end{cases}$$

and  $z$  being the axial coordinate of the interaction of the annihilation photon, with origin at one end of the crystal bar of length  $L_C$ .

The *effective* light absorption length  $\lambda$  is different from the bulk absorption length  $\lambda_b$  as it accounts for the real path length of the photons, which is increased due to the multiple bounces:  $\lambda = k \cdot \lambda_b$ . The geometrical parameter  $k = z / \langle \text{path length} \rangle$  depends on the refractive index of the scintillator and has been determined for LSO and LaBr<sub>3</sub> in the M.C. code as  $\approx 0.7$ .

The spatial distribution of the photoelectrons over the segmented silicon sensor is shown in fig. 15. About 70% of the photoelectrons of a hit crystal bar are detected by the associated sensor pad, while the rest is spread over the closest adjacent pads in a well defined pattern. Expressed in terms of energy, a 511 keV photon will deposit on an adjacent pad not more than the equivalent of about 30 keV.

**4.2. Energy resolution.** – The energy resolution  $R = \Delta E / E$  (FWHM), with which the photon energy can be measured, is the quadratic convolution of three contributions:

$$(3) \quad R = R_{\text{sci}} \oplus R_{\text{stat}} \oplus R_{\text{noise}}.$$

The intrinsic resolution of the scintillator  $R_{\text{sci}}$  due to material inhomogenities, impurities etc. was derived from ref. [23] by convolving the statistical fluctuation term as  $R_{\text{sci}} = 6.2\%$  and  $1.2\%$  for LSO and LaBr<sub>3</sub>, respectively (see table I).  $R_{\text{stat}}$  accounts for the statistical fluctuation involved in the light generation, transport and detection process

$$(4) \quad R_{\text{stat}}(\text{FWHM}) = 2.35 \sqrt{\frac{1.09}{N_{\text{p.e.}}}}$$

and includes the Excess Noise Factor of the HPD  $ENF = 1.09$ .

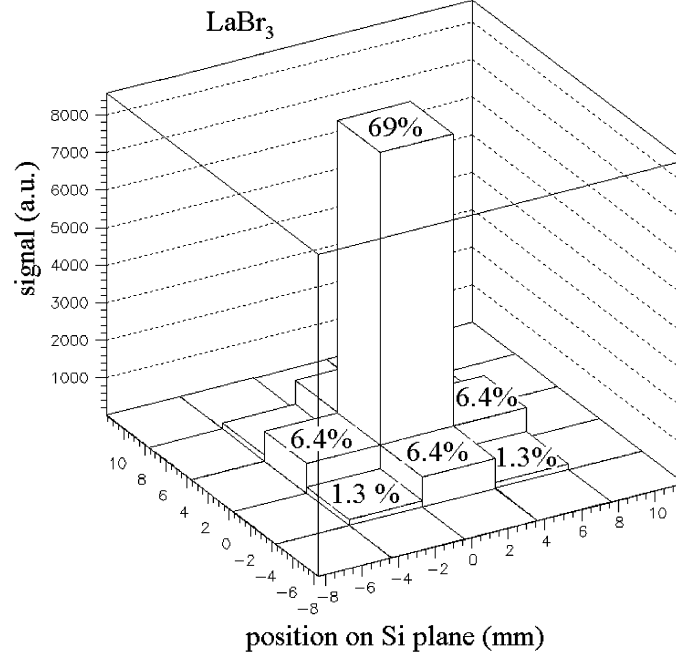


Fig. 15. – Simulated distribution of the hit map on the silicon sensor for the readout of a scintillator crystal centred over the central Si pad.

The contribution due to noise in the electronic detection chain including the photodetector (amplifier, shaper, ADC, ...) is negligible for HPDs. With an Equivalent Noise Charge (ENC) of about  $10^3 \text{ e}^-$ , the noise term becomes

$$(5) \quad R_{\text{noise}}(\text{FWHM}) = \frac{2.35 \cdot 10^3}{N_{\text{p.e.}} \cdot M} \approx 10^{-3},$$

where  $M \approx 10^3$  is the gain of the HPD at  $U_C = 12 \text{ kV}$ .

The full energy resolution (according to eq. (3)) at  $E = 511 \text{ keV}$  is therefore 9% and 3.2% (FWHM) for LSO and  $\text{LaBr}_3$ , respectively.

**4.3. Reconstruction of the interaction point of the annihilation photon.** – The coordinates of the photon interaction point in the transaxial  $(x, y)$ -plane are derived from the address of the hit crystal bars forming the scintillator matrix. The resolution  $\sigma_x$  ( $\sigma_y$ ) is determined by the cross-section of the bar

$$(6) \quad \sigma_x = \sigma_y = \frac{s}{\sqrt{12}},$$

where  $s = 3.2 \text{ mm}$  is the width of the square crystals. The  $x$  and  $y$  coordinates of the photon interaction points can thus be localized with a precision of 2.2 mm (FWHM). Consequently the spatial resolution of the reconstructed positron annihilation point is in

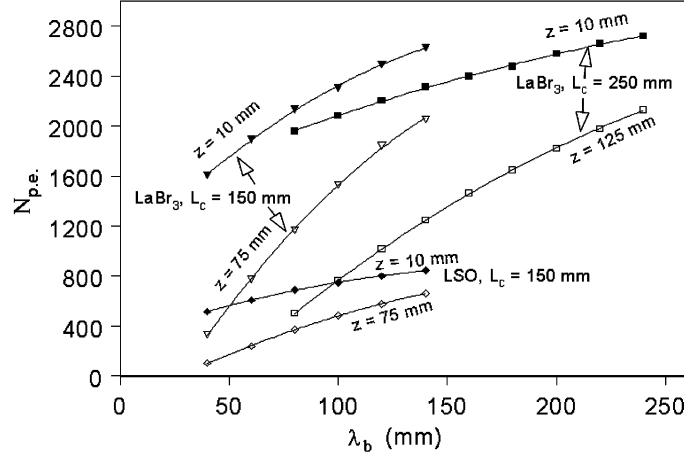


Fig. 16. – Variation of the number of detected photons with the bulk absorption length of the scintillator crystal.

first order given by

$$(7) \quad \sigma_x^{\text{rec.}} = \sigma_y^{\text{rec.}} = \frac{1}{\sqrt{2}} \sigma_x, \sigma_y = \frac{s}{\sqrt{24}} \approx \frac{s}{2} (\text{FWHM}).$$

This approximation is strictly valid for a source centred in the transverse field of view, independent of the axial coordinate.

The axial coordinate  $z$  of the photon interaction is derived from the measurement of the number of photoelectrons ( $N_1, N_2$ ), detected at the two ends of the crystal bars.

$$(8) \quad z = \frac{1}{2} \left[ \lambda \cdot \ln \left( \frac{N_1}{N_2} \right) + L_C \right].$$

Error propagation w.r.t. the fluctuations of  $N_1$  and  $N_2$  (ignoring again the very small influence of electronics noise) leads to the measurement precision<sup>(10)</sup>

$$(9) \quad \sigma_z = \frac{\lambda}{\sqrt{2N_0}} [ENF(e^{z/\lambda} + e^{(L_c-z)/\lambda})]^{1/2}$$

and  $\sigma_z^{\text{rec}} \approx \sigma_z / \sqrt{2}$ .

**4.4. Monte Carlo simulations of the light transport.** – The above-mentioned Monte Carlo code allows to track scintillation photons individually from creation to detection. The code takes into account refraction and reflection at all optical interfaces (crystal/air, crystal/photodetector window), reflection and absorption losses as well as photodetector characteristics like quantum efficiency, point spread function and segmentation. The

<sup>(10)</sup> Equation (9) ignores the contribution of pathlength fluctuations. Those are however accounted for by the M.C. calculations described in the next section.

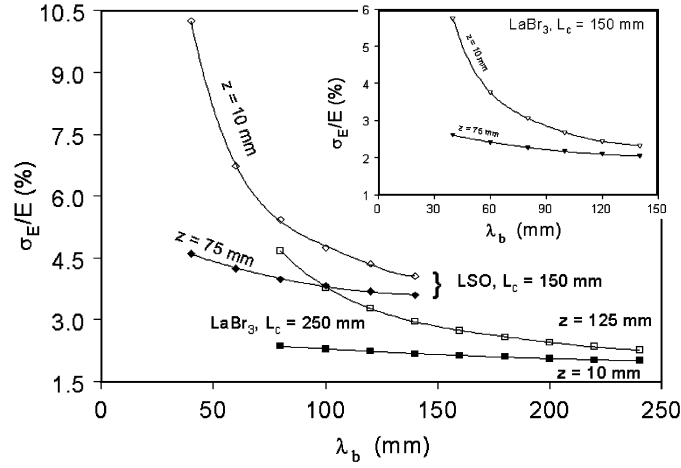


Fig. 17. – Dependence of the statistical term of the energy resolution ( $E = 511$  keV) on the bulk absorption length of the scintillator crystal.

code allows to assess spatial and energy resolution and their variation with material and geometrical parameters and also provides an independent cross-check of the above derived analytical expressions.

4.4.1. The influence of the bulk absorption length  $\lambda_b$ . The axial geometry with long scintillator crystals requires to choose the crystal bulk absorption length  $\lambda_b$  in relation to the length of the crystal  $L_C$ , in order to define an optimal compromise between achievable energy and  $z$ -resolution.

Figures 16, 17 and 18 show simulation results for LSO ( $L_C = 150$  mm) and LaBr<sub>3</sub> crystals ( $L_C = 150$  and 250 mm), with  $\lambda_b$  as free parameter. For every configuration

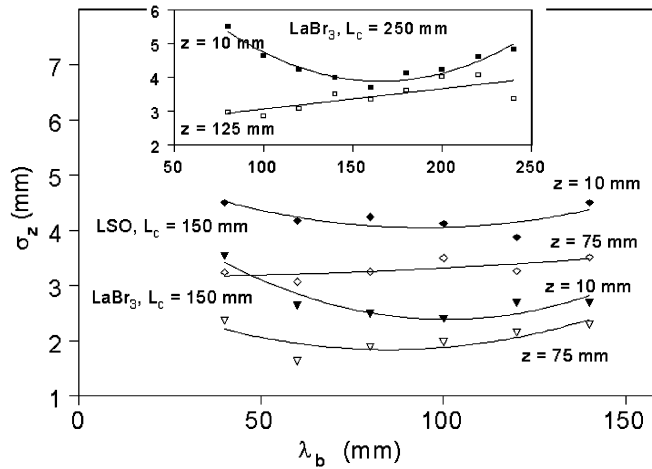


Fig. 18. – Dependence of the expected axial ( $z$ ) resolution for single photons ( $E = 511$  keV) on the bulk absorption length of the scintillator crystal.

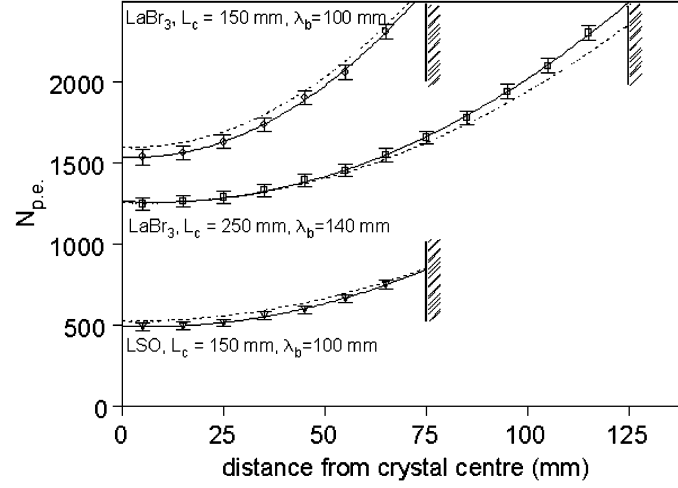


Fig. 19. – Variation of the detected number of photoelectrons ( $E = 511$  keV) with the detection point along the crystal  $z$ -axis. Note that in figs. 19 to 21 the distance is measured from the crystal centre and not from the crystal end.

light emission at  $z_{em} = 10$  mm and  $z_{em} = L_c/2$  has been simulated, while  $x_{em}$  and  $y_{em}$  were varied uniformly  $0 \leq x, y \leq 3.2$  mm. As good compromise appear 150 mm long crystals (LSO or LaBr<sub>3</sub>) with  $\lambda_b \approx 100$  mm. For 250 mm long LaBr<sub>3</sub> crystals  $\lambda_b$  values around 140 mm give the best overall results. The lower light yield of LSO would lead to poor resolutions for 250 mm long crystals. This configuration was therefore discarded.

With these  $\lambda_b$  parameters the achievable energy and spatial resolution has been investigated as a function of the axial emission point  $z_{em}$ .

Figure 19 shows the number of photoelectrons, detected by the two HPDs as a function

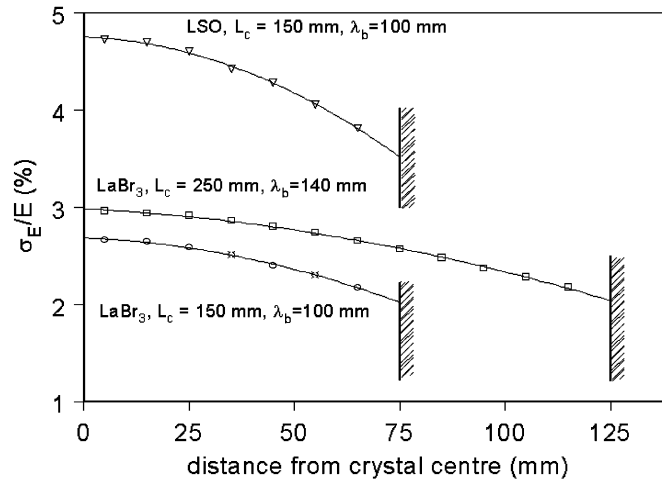


Fig. 20. – Dependence of the single gamma energy resolution (only statistic term,  $E = 511$  keV) on the  $z$ -coordinate.

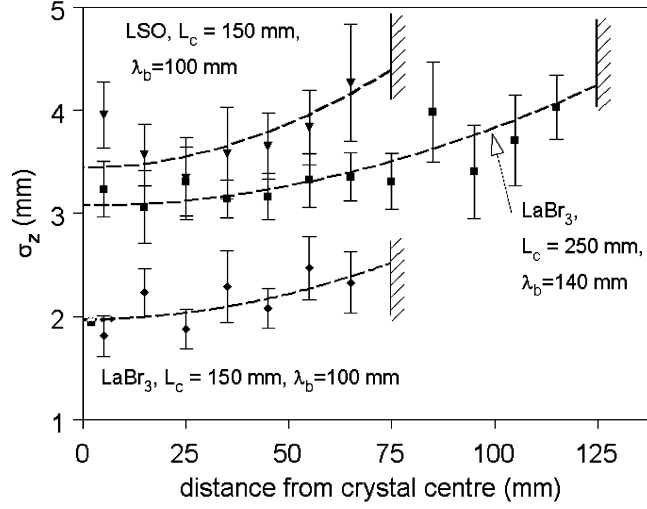


Fig. 21. – Dependence of the axial spatial resolution (single photons,  $E = 511$  keV) on the  $z$ -coordinate. The dashed lines correspond to the analytical formula (eq. (9)) multiplied by an empirical factor 1.13. The correction factor is required to account for the pathlength fluctuations which are not included in the analytical expression.

of the emission point  $z$ . For comparison the results of the analytical calculation (dashed lines, according to eq. (1)) are shown together with the M.C. data, revealing a small but systematic discrepancy. The analytical calculations are made with a constant value of  $\epsilon_{TT}$ , while in reality  $\epsilon_{TT}$  depends slightly on the emission position. This is a pure geometrical effect and is due to the increasing fraction of scintillation photons which can directly hit the photodetector without prior reflection from the crystal side faces. The maximum difference is about 5%. The number of detected photons and the  $z$  coordinate depend strongly on the effective light absorption length  $\lambda$  (see eqs. (1) and (8)). For an accurate reconstruction of the energy and interaction point of the annihilation photon, the effective light absorption length  $\lambda$  of all crystal bars needs to be determined experimentally, in order to cope with production related variations. In the annex we describe a simple procedure to measure  $\lambda$  with a precision on the percent level. The statistical term of the energy resolution ( $\sigma_{E_{stat}}/E$ ) and the spatial axial resolution  $\sigma_z$  are plotted in figs. 20 and 21, again as function of the emission point  $z$ . For the  $\text{LaBr}_3$  crystals the simulations predict excellent values in both respects. An energy resolution according to eq. (3) of about 6-6.5% (FWHM) seems to be achievable. The axial spatial resolution  $\sigma_z$  is of the order 2 mm (150 mm) and 3 mm (250 mm long crystals), predicting an axial resolution of the positron annihilation point of 3.3 and 5 mm (FWHM), respectively. The statistical term of the LSO energy resolution is somewhat worse, however still matches the intrinsic resolution. The axial spatial resolution is also inferior compared to  $\text{LaBr}_3$ .

**4.5. Spatial reconstruction resolution—Comparison with a conventional radial PET geometry.** – Basic M.C. simulations have been performed to assess the achievable reconstruction resolution. We compare the spatial (volumetric) reconstruction resolution of the proposed axial concept with published HRRT data and simulation results of a classic (HRRT-like) radial scintillator arrangement.

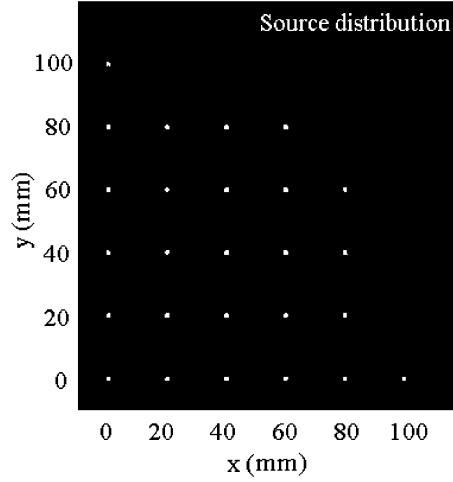


Fig. 22. – Distribution of the pointlike sources ( $1 \times 1 \times 1 \text{ mm}^3$ ) in the transaxial  $(x, y)$ -plane at  $z = 0$ .

For a simple and clear interpretation of the results, the simulations only consider photoelectric interactions of 511 keV photons disregarding Compton scatterings in the organic tissue and in the scintillator matrices. The contribution of the scatter events to the HRRT performance is difficult to be interpreted because of the lack of detailed information on the data processing from the readout of the phoswich layers. However, as it will be shown, even in these conditions, the comparison between the simulations and the published HRRT experimental data allows a good understanding of the responses.

The M.C. code starts off with a pattern of small  $1 \times 1 \times 1 \text{ mm}^3$ , *i.e.* quasi pointlike, positron sources. The range of the positrons in the organic tissue (a Gaussian distribution of 0.5 mm (FWHM) for the  $^{18}\text{F}$  radiotracer) and the non-collinearity of the 511 keV

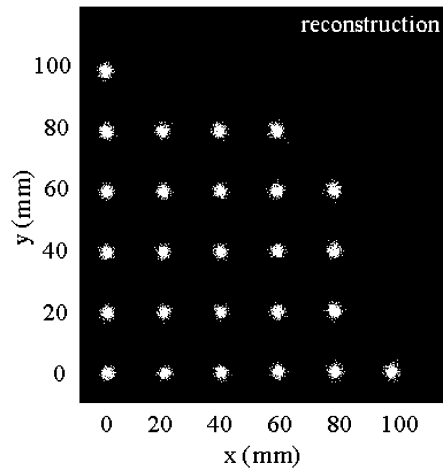


Fig. 23. – Reconstruction of the source distribution in the transaxial  $(x, y)$ -plane at  $z = 0$ .

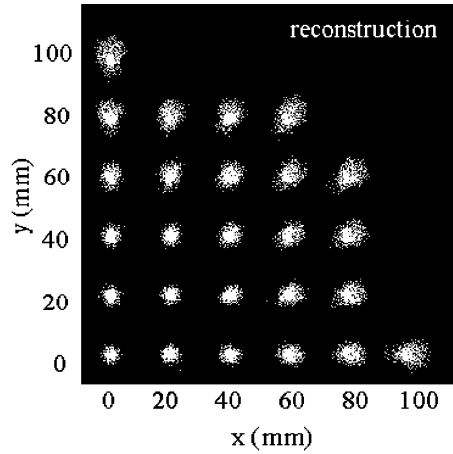


Fig. 24. – Similar to fig. 23, however for a radial arrangement of 30 mm long crystal.

annihilation photons ( $180 \pm 0.25^\circ$ ) are accounted for. Both the path of the positron and the emission direction of the annihilation photons follow an isotropic distribution. A scanner based on the axial geometry with a free inner diameter of 320 mm was simulated using crystals of  $3.2 \times 3.2 \text{ mm}^2$  width and 150 mm (LSO) and 250 mm ( $\text{LaBr}_3$ ) length. For the  $z$ -resolution the crystals were assumed to have a bulk light attenuation length of 100 mm and 140 mm, respectively.

The scanner based on a radial geometry consists of a circular ( $\varnothing_{\text{int.}} = 46.8 \text{ cm}$ ) arrangement of LSO crystals of  $2.1 \times 2.1 \times 30 \text{ mm}^3$  size. This geometry differs of the

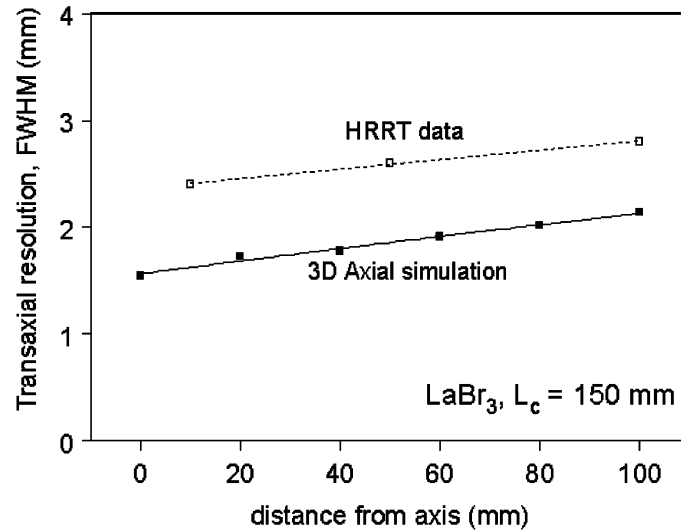


Fig. 25. – Resolution of spatial reconstruction in the transaxial ( $x - y$ )-plane. The simulation results are for  $\text{LaBr}_3$  crystals of 150 mm length. The HRRT data has been extracted from ref. [12].



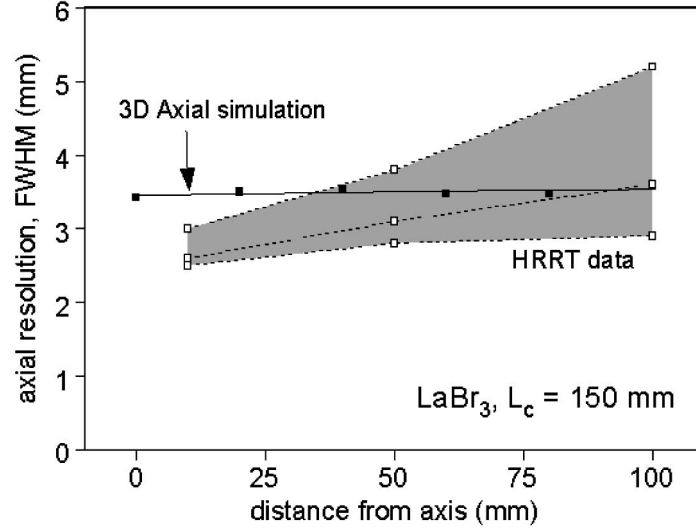


Fig. 26. – Resolution of spatial reconstruction in the axial ( $z$ ) plane. The simulation results are again for  $\text{LaBr}_3$  crystals of 150 mm length. The grey shaded area corresponds to HRRT data (ref. [12]) obtained in different operation and reconstruction modes.

octagonal shape of the HRRT but should not alter too much the interpretation of the results. The photon conversion point in a hit crystal is assumed at half the crystal length.

The trajectories of the annihilation photons are extrapolated from the source to the sensitive volume. The detection points are determined according to the attenuation length and the segmentation of the sensitive volume. The line of response (LoR) is then drawn between the two detection points.

To avoid the complication of a real tomographic reconstruction, the resolution is obtained by calculating analytically the shortest distance between the line of response and the original positron emission point. The projections of this distance in the  $x$ - $y$  (transaxial) and  $z$  (axial) direction are accumulated in histograms and fitted by Gaussian curves. Their width corresponds to the resolution searched for.

An empirical multiplication factor of 1.25 [50] is applied to the results in the transaxial plane to account for the additional uncertainty which the tomographic reconstruction procedure would introduce. As the proposed axial geometry uses individual crystal readout, a block decoding scheme (Anger logic), which would lead to further resolution degradation ( $\approx 2.2\text{mm}$  (FWHM) added in quadrature [50]), is not necessary.

Small sources of  $1 \times 1 \times 1 \text{ mm}^3$  were simulated at coordinates equidistantly distributed ( $x_i, y_i = 0, 2, 4, 6, 8, 10 \text{ cm}$ ) over the transverse FOV. Figures 22, 23 and 24 show examples of the original and reconstructed distributions in the transaxial plane for  $z = 0$ .

Figures 25 and 26 show the results of the simulations with the published data of the HRRT [12, 13], see also table II. The resolutions are derived from Gaussian fits to the distributions of the  $x$ - $y$ —in the transaxial plane—and  $z$  projections of the shortest calculated distance between the reconstructed LOR and the true positron annihilation point.

For illustration purposes the same source configuration has been simulated and reconstructed for a HRRT-like radial geometry with crystals of 30 mm length (see fig. 24). At

TABLE II. – Comparison of reconstruction resolution (FWHM values): HRRT data vs. HPD-PET simulation. In the simulations a crystal length of 150 mm was assumed. All values correspond to the central plane ( $z = 0$ ).

	Transaxial resolution (mm)		Axial resolution (mm)		Mean volumetric resolution (mm <sup>3</sup> ) $R_V = R_x \times R_y \times R_z$
	$R_x (= R_y)$ $x = 0; \quad x = 100;$ $y = 0 \quad y = 0$		$R_z$ $x = 0; \quad x = 100;$ $y = 0 \quad y = 0$		
HRRT data, span 9	2.35	2.75	2.5	3.6	20
HRRT data, span 3	2.35	2.75	2.5	2.8	18
HPD-PET LSO	1.85	2.35	5.78	6.33	26
HPD-PET LaBr <sub>3</sub>	1.59	2.13	3.43	3.57	11.8

10 cm from the centre of the FOV, and without DOI measurement (Phoswich technique not employed), the parallax error in the transaxial plane is sizable and gives rise to a clear astigmatism.

The comparison of the HRRT experimental resolutions with the simulations is more difficult to analyze in the absence of detailed information on the data processing. In the transaxial plane, at the centre of the FOV there is a difference of about 35% between the data and the simulations which can be explained by the contribution of Compton interactions in the scintillator blocks. At 10 cm off centre, the agreement is good because the dominant contribution to the resolution is the parallax error well accounted by the simulation. For the axial  $z$  coordinate, the conclusion of the comparison is inverted. At the centre of the FOV the agreement is good within the errors. At 10 cm off centre the deviation strongly depends on the axial data compression, characterized by span and ring difference which determine the maximum angular acceptance.

As the Compton events are clearly reconstructed with the axial PET concept, one must compare the M.C simulations with the experimental data of the HRRT. At the centre of the FOV ( $x = 0$ ), the resolution has the expected value, independently of the crystal choice, but degrades by about 40% at  $x = 10$  cm because of the asymmetry of the LOR with respect of the emission point. As previously stressed, the high photon yield of LaBr<sub>3</sub> crystals significantly improves the axial resolution.

With 15 cm long LaBr<sub>3</sub> crystals a mean volumetric reconstruction resolution of 11.8 mm<sup>3</sup> is attainable, hence about 40% better than the HRRT measured one. For 15 cm long LSO crystals the expected resolution is about 14% worse than the HRRT results. This last performance would obviously improve by a factor 0.86 if LSO would be replaced by LYSO crystals with a photon yield of 35 ph/keV in addition by a factor 0.85 by increasing the photocathode quantum efficiency from 18 to 25%.

## 5. – Detection efficiency for *true* PET events

In this section we discuss, from a physics point of view, the detection efficiency of True (T) events for photon incidence normal to the scintillator array. The values thus obtained are characteristic of the matrix configuration and of the scintillating material, independently of the scanner geometry.

A True event is defined as the detection of two annihilation quanta of 511 keV energy emitted in opposite directions and which undergo either a photoelectric conversion or a Compton scattering in the matrix of scintillators which, unambiguously, can be

TABLE III. – *Comparison of detection efficiencies: HRRT vs. PET-HPD (at normal incidence).*

Detector Detector depth	LSO:Ce		LaBr <sub>3</sub> :Ce	
	HRRT 15 mm	3D axial 41.2 mm	3D axial 51.2 mm	- $\infty$
Single photon efficiencies				
a) Photoelectric	21.4%	30%	13.8%	15%
b) $C \rightarrow pe$	4.8%	5.7%	3.4%	
c) $C \rightarrow C \rightarrow pe$	4.8%	4%	2.6%	
d) $C \rightarrow$ absorption		12.6%	12.3%	$\sim 21\%$
i) a+b+c	26.2%	39.7%	19.8%	
ii) a+d $\rightarrow$ absorption		42.6%	26.1%	$\sim 36\%$
Photon pair efficiencies				
i) a+b+c	6.9% <sup>(1)</sup>	15.7%	3.9%	
ii) a+d		18.1%	6.8%	$\sim 13\%$
Ratio HPD-PET / HRRT				
i) a+b+c		2.3	0.6	
ii) a+d		2.6	1	
Compton enhancement		$\sim 2.0$	$\sim 2.5$	

<sup>(1)</sup> HRRT data. For pure photoelectric events a photon pair efficiency of 4.6% would be expected. We conclude that the HRRT events contain a substantial fraction of events with Compton interactions.

reconstructed.

The results which are given in table III are derived from analytic calculations and suffer from inevitable approximations. Their validity, however, was tested for a matrix of LSO crystals with a M.C simulation using GEANT 4 code. Agreement was found within about  $\pm 10\%$  error. The detection efficiencies are rather underestimated, but allow a coherent comparison of the expected performances with those of the HRRT-PET scanner.

The values of photon cross-sections, attenuation and absorption lengths for 511 keV photons are listed in table I, and were derived by interpolation from the Hubbel tables of the National Institute of Standards and Technology.

**5.1. Detector Compton scattering: Reconstruction and limitations.** – In order to unambiguously distinguish the coordinates of the primary Compton interaction of those of the secondary interactions (photoelectric conversion or Compton scattering) the reconstruction program restricted to events in which the photon of the primary Compton scattering is emitted in the forward direction.

We have used as selection criteria, the Klein-Nishima formulation which describes the kinematics and the cross-section dependence with the incident photon energy and scattering angle  $\theta_C$  (see figs. 27 and 28).

A detailed analysis shows that the scattering angle in the forward hemisphere must be restricted to  $0 < \theta_C < 60^\circ$  if the energy of the recoil electron in the primary interaction is below 170 keV for 511 keV photons. About 60% of all scatter events fall in this category. However, for reconstructing with an acceptable precision the  $z$  axial coordinate a minimum recoil electron energy of 50 keV is required, a limit which conceptually is not needed for the reconstruction in the transaxial plane. Finally, the acceptance in energy

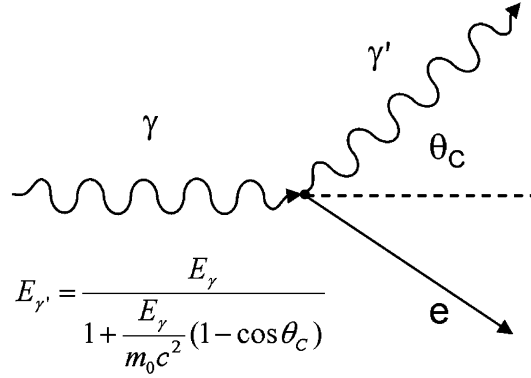


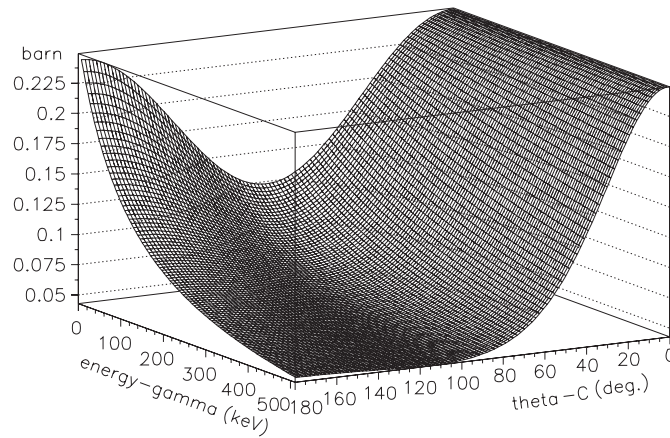
Fig. 27. – Kinematics of the Compton interaction.

between 340 and 460 keV of the scattered photon reduces to about 25% the fraction of scatter events which unambiguously can be reconstructed.

**5.2. Estimation of the detection efficiency.** – If  $\lambda_{\text{att}}$  is the attenuation length of incident 511 keV photons, the probability of interaction in a scintillator of thickness  $t$  is  $1 - \exp(-t/\lambda_{\text{att}})$  and the mean depth of interaction  $\langle DOI \rangle = \lambda_{\text{att}} - t/(\exp[t/\lambda_{\text{att}}] - 1)$ . Therefore, the residual mean path for a photon emitted in the forward direction is simply  $\langle t_{\text{res}} \rangle = [t/(1 - \exp[-t/\lambda_{\text{att}}] - \lambda_{\text{att}})]/\cos(\theta_C)$ . Hence the probability of a 2nd interaction (photoelectric or Compton int.) in  $\langle t_{\text{res}} \rangle$  is  $1 - \exp[-\langle t_{\text{res}} \rangle/\lambda_{\text{att}}(E_C)]$ , and the probability of a full absorption  $1 - \exp[-\langle t_{\text{res}} \rangle/\lambda_{\text{abs}}(E_C)]$ .

The results shown in table III have been obtained assuming a mean photon energy in the primary Compton interaction of 400 keV.

In table III two selection criteria of unambiguously reconstructed Compton events are given. For the first criteria a scatter event is selected as T if the scattered photon undergoes a secondary photoelectric conversion, whilst for the second criteria an event

Fig. 28. – Cross-section for Compton interaction as function of scattering angle  $\theta_C$  and photon energy.

is taken as T if the total energy is lost in the scintillator matrix.

A sensitivity of 4.4 cps/kBq has been measured for the HRRT [11] with a phantom of 20 cm in diameter and 20 cm in length, in conformity with the standard NEMA-NU2 test protocol. However, according to M.C simulations of the HRRT (see next par.) one expects a sensitivity of 2.9 cps/kBq for the detection of two coincident photons that underwent a photoelectric effect. The difference can be understood by the detection of Compton scattered events which develop in a single scintillator block and, for part, are not rejected by their detection in both phoswich layers. This scatter events enhance the detection efficiency for two coincident annihilation photons from 4.6 to 6.9% (see table III).

Note that for the axial PET-HPD we assume a total scintillator thickness of 41.6 mm for LSO crystal bars, hence 13 layers of 3.2 mm according to the design discussed in subsect. 3.1, and 51.2 mm ( $16 \times 3.2$  mm) for LaBr<sub>3</sub> corresponding to a 90° rotation of the previous matrix configuration.

Equipped with LSO (LYSO) scintillators the intrinsic detection efficiency of the PET-HPD matrix is expected to be a factor about 2.5 higher than the one of the HRRT.

Because the photofraction of LaBr<sub>3</sub> is a factor twice lower than the one of LSO the Compton enhancement is dominant but, as it can be seen, the detection efficiency is lower. As the attenuation length of LaBr<sub>3</sub> crystal is long compared to LSO, their use requires a larger matrix volume hence a significant increase of the cost.

**5.3. PET sensitivity and NEMA-NU2 protocol of characterization.** – The sensitivity, *i.e.* the True event rate T per activity (cps/kBq), and the scatter fraction ( $SF = S/(S + T)$ ) have been estimated in the conditions of the NEMA-NU2 test protocol using a phantom of 20 cm in diameter and 20 cm long filled with a dilution of <sup>18</sup>F in water. *S* denotes the event rate involving photons which underwent Compton scattering in the patient (or phantom).

Usually measurements of the dependence of the Noise Equivalent Count rate  $NEC = T^2/(T + S + R)$  on the electronic dead time are made with activity concentrations up to 1 or 1.5  $\mu$ Ci/ml. *R* describes the rate of random coincidences.

M.C simulations of the NEMA experimental test configuration have been performed for the PET-HPD and the HRRT scanners to determine the respective solid angle for detection of T events. The mean value of the acceptance ( $\Delta\Omega/4\pi$ ) thus estimated is 0.165 for the axial PET design with 150 mm long crystals and 0.344 for the HRRT, respectively.

The photon mean free path calculated from the distribution of the path lengths inside the phantom for detected photons is 8.55 cm. Therefore, for a photon attenuation length of 10.3 cm in water ( $\mu_{att}(511 \text{ keV}) = 0.097 \text{ cm}^{-1}$ ) the probability of a True event to escape the phantom is  $\exp[-17.1/10.3] = 0.19$ .

Taking the detection efficiencies listed in table III one can estimate a PET-HPD sensitivity of 2.7 and 5.5 cps/kBq without and with Compton enhancement respectively.

For the HRRT, as already quoted, a sensitivity of 4.4 cps/kBq is estimated from a measurement of *S* + *T* events, by assuming according to the authors a *SF* of 0.4, which suggests the detection of Compton events but with a limited degradation of the spatial resolution.

TABLE IV. – *Performance summary and comparison.*

	HRRT	PET-HPD					
Scintillator	LSO:Ce	LSO:Ce			LaBr <sub>3</sub> :Ce		
AFOV (mm)	250	150			150		
Detector depth (mm)	15	41.2 (13 × 3.2)			51.2 (16 × 3.2)		
$\Delta\Omega/4\pi$	0.344	0.165			0.165		
$\epsilon_{\text{det}}(2 \text{ photons}) (\%)$	measured	PE	Compton	total	PE	Compton	total
	6.9	8.5	7.2	15.7; 18.1	1.9	4.9	6.8
$\Delta E/E$ (511 keV) (%)	17	10.3( $z=0$ ), 12.4( $z=L/2$ )			4.7( $z=0$ ), 5.3( $z=L/2$ )		
$\Delta V$ (mm <sup>3</sup> )	20	22	~ 45	~ 33	11	~ 22	~ 18
$\Delta E/E \cdot \Delta V$ (%·mm <sup>3</sup> )	340	250	~ 510	~ 370	55	~ 110	~ 90
$FoM^{(1)}$	0.7	0.6	0.25	0.8	0.6	0.74	1.25
Compton enhancement				1.85			2.8
sensitivity (cps/kBq)	4.4	2.7	2.8	5.5	0.6	1.0	2.1

<sup>(1)</sup> Figure of Merit  $FoM = \epsilon_{\text{det}}(2 \text{ photons}) \cdot \frac{\Delta\Omega}{4\pi} \cdot \left(\frac{\Delta E}{E} \cdot R_V\right)^{-1} (\text{mm}^{-3})$ .

## 6. – Figure of merit: Estimate and comparison

We define a figure of merit as

$$(10) \quad FoM = \epsilon_{\text{det}} \cdot \frac{\Delta\Omega}{4\pi} \cdot QF,$$

where  $\epsilon_{\text{det}}$  is the detection efficiency for  $T$  events and  $\Delta\Omega/4\pi$  describes the acceptance of the scanner. We introduce the quality factor  $QF = \left(\frac{\Delta E}{E} \cdot R_V\right)^{-1}$  as a combination of energy and spatial resolution, which to a certain extent characterizes the achievable image contrast. The quantity  $FoM$  can therefore serve for a global characterization of the *overall technical performance*. The impact of the running conditions on the image contrast through the detection of scatter events ( $S$ ) in the organic tissues and of random coincidences ( $R$ ) is obviously ignored in this simple approach. While the  $S$  rate depends on the discrimination in energy of the detected photons, the  $R$  rate is determined by the width of the coincidence time window. This aspect is discussed in the next section devoted to data acquisition (DAQ) system.

The comparative results are shown in table IV.

Because of the low recoil electron energy, the axial resolution of the reconstructed Compton events degrades, worsening the spatial resolution DV. However, despite an acceptance a factor 2 lower than the HRRT, the merit factor of the PET-HPD with LSO scintillators is comparable but it is about 70% higher with LaBr<sub>3</sub>.

It must be noticed that the quality factor  $QF$  varies roughly proportionally to the number of detected photoelectrons. Therefore, if a light yield of  $35 \cdot 10^3$  photons/MeV (LYSO) is attainable and by improving the photocathode quantum efficiency at 420 nm from 18 to 25% (standard commercial value), the figure of merit of the discussed 3D axial PET could be two times larger than the one of the HRRT. A design with 25 cm long LaBr<sub>3</sub> crystal bars does not allow an improvement of the figure of merit despite the increase of the acceptance because of the spatial and energy resolution degradation. The

TABLE V. – *Trigger selection criteria and DAQ rates.*

Si sensor back plane readout		no			yes, $E_\gamma \geq 400$ keV
Energy threshold <i>FOR</i>		50 keV	50 keV	400 keV	50 keV
Selection: hit multiplicity		any	$m \leq 2$	$m = 1$ (photo-peak)	any
Phantom activity	interaction type	<i>relative count rate</i> (cps/kBq)			
Low <sup>(1)</sup>	single $\gamma$ (PE + Compton)	280	115	49	
	2 coincident $\gamma$ s (PE + Compton)	90	$\sim 18$	$\leq 3$	
	DAQ rate	90			6-7
		<i>absolute count rate</i> (cps = Hz)			
81.4 MBq <sup>(2)</sup>	DAQ rate (8 parallel DAQ chains)	$7.3 \cdot 10^6$ Hz			$5\text{--}6 \cdot 10^5$ Hz
81.4 MBq	accidental's rate (CTW = 10 ns)	$\sim 1.2 \cdot 10^6$ Hz			$\sim 10^5$ Hz

<sup>1)</sup> Random count rate is negligible.

<sup>2)</sup> 81.4 MBq = 0.35  $\mu$ Ci/ml  $\times$  6310 ml.

intrinsic *FoM* is, obviously, affected by the performances of the FE electronic and the DAQ system which determine the image contrast ( $\sim T/(T + S + R)$ ) as a function of the operating environment (radioactivity), and consequently the NEC rate  $T^2(T + S + R)$ .

## 7. – Data acquisition

**7.1. Principle and limitations.** – The principle of the data acquisition (DAQ) system and its particular features are driven by two main constraints: i) the readout architecture of the VATA front-end chip and ii) the requirement to detect and analyze photon interactions, which involve Compton scattering in the detector.

The tracking of the latter interactions requires to run the FE electronic with a relatively low detection threshold of about 50 keV/channel in order to detect and reconstruct the recoil electron of the primary Compton scattering. However, the low threshold prevents the rejection of a large fraction of photons which underwent Compton scattering in the organic tissue. Such discrimination is used in all conventional PET systems, as it allows to drastically decrease the counting rate and thus also reduces the rate of accidental coincidences.

In the so-called *sparse readout mode*, the VATA readout sequence consists of a multiplexed sequential readout of only those channels with a hit (see subsect. 3.4). The front-end chip can be operated at a clock speed of 20 MHz. This leads to a mean readout time of  $\approx 1.2\mu$ s per event, depending somewhat on the selection criteria applied to the hit multiplicity. Without a stringent selection of events, the electronic dead time would paralyze the readout system already for modest source activity levels and hence spoil the sensitivity of the PET scanner.

It is a unique and intrinsic property of the HPD photodetector which allows to resolve this problem. The HPD provides a fast measurement of the total energy deposited in the scintillator matrix. The total energy information is derived from the induced signal on the Si sensor back plane which, as it covers the full detector area, is proportional to the total amount of charge deposited in the Si sensor, and hence to the total energy converted in the scintillator block. As will be detailed below, the large and prompt back plane signal allows to identify and reject low energy photons (from Compton scattering in the patient), without compromising the ability of the FE electronic to detect Compton

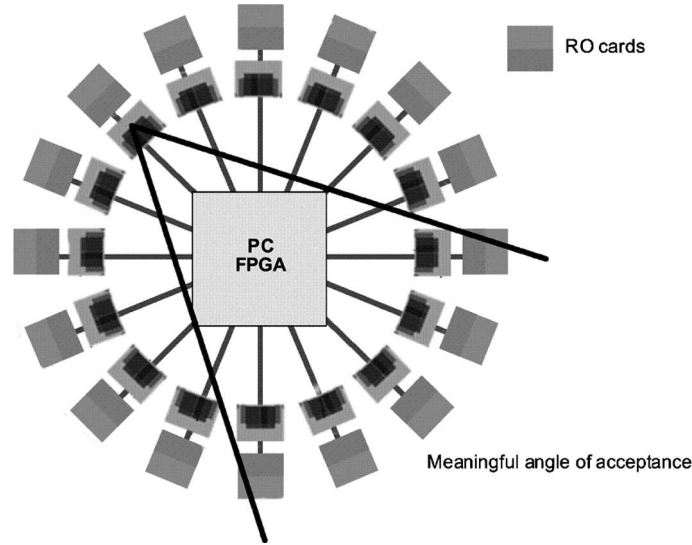


Fig. 29. – Schematic representation of the 16 readout modules. For each of the modules a geometrical acceptance range is defined in which coincidences with other modules can be formed.

interactions in the scintillator matrix. This is an essential and fundamental feature of our approach and the proposed DAQ concept.

To better understand the limitations of the DAQ, table V shows the dependence of the trigger rates with various event selection criteria, like energy threshold for the generation of a Fast OR (*FOR* signal) and multiplicity of crystal clusters. The numbers were estimated in the conditions of the NEMA-NU2 test protocol from M.C simulations and analytic calculations, within  $\pm 10\%$  error. The rate of accidentals was estimated on the basis of a Coincidence Time Window (CTW) of 10 ns for a phantom radio-tracer concentration of  $0.35\mu\text{Ci/ml}$  ( $V = 6310\text{ ml}$ , *i.e.* total activity = 81.4 MBq).

Operating the FE electronic with a detection threshold of 50 keV without additional event selection would require a huge and technically unfeasible DAQ rate. The conditions improve significantly when applying a cut-off on the hit multiplicity and, obviously, drastically, if the detection threshold is raised to 400 keV (right most column in table V), a value which greatly favors the detection of unscattered photons of 511 keV.

Running with a detection threshold of 50 keV, which enables *Compton sensitivity enhancement*, and exploiting at the same time the total energy information from the Si sensor back plane, leads to a reduction of the DAQ rate by a factor of about 14. However, even in these conditions, a reasonably achievable DAQ rate of 0.5 to 0.6 MHz would result in a poor acquisition efficiency of about 50%. Therefore, as described below, the DAQ system is split in several parallel and independent chains. In the following we discuss a 3D axial PET scanner comprising 16 modules.

Note that for an activity of 81.4 MBq the count rate of the *FOR* signal is of the order 1.9 MHz/module but decreases to 0.7 MHz/module for a threshold setting of 50 keV.

For  $N_m = 16$  modules covering the azimuthal acceptance, there are  $N_m \cdot (N_m - 1)/2 = 120$  possibilities to form module pairs. From the geometrical point of view, only roughly half of them will lead to physically meaningful coincidences (*T* and *S* events), but all of them will contribute to the random rate (*R*). To minimize these accidentals the



DAQ architecture is designed to accept coincidences of hit modules only within a limited angular acceptance, *e.g.*, five or six modules in the opposite hemisphere (see fig. 29). The DAQ system thus searches for coincidences between a given module and, for example, the 5 or 6 opposite modules. This reduces the number of valid module combinations and consequently the associated accidentals rate by more than a factor 2.

This *selective pair approach* allows to structure the DAQ architecture as 8 coincidence chains, which are defined dynamically and work in parallel in an independent and asynchronous way. A coincidence chain consists of a first module and a dynamically associated second module from the opposite hemisphere. When a chain detects two module pairs in coincidence, all other modules are unaffected and stay armed for other coincidences.

The detection of randoms  $R$  is strongly suppressed w.r.t.  $T$  and  $S$  events by requiring coincidences of exactly two modules. The fast response of the sensor back plane is exploited for the search of coincidences between modules allowing a time resolution of 5 to 10 ns. The randoms rate due to uncorrelated single photons simulating  $T$  events decreases by a factor of about ten after energy discrimination, but still constitutes about 20% of the acquired data. The estimated image contrast  $T/(T + S + R)$  is about 0.75 (assuming a phantom activity of  $0.35 \mu\text{Ci/ml}$  and a DAQ efficiency of  $> 0.95$ , compared to 0.4 for the HRRT. Under these conditions the NEC value has been estimated to  $3 \cdot 10^5$  cps, roughly twice the value quoted for the HRRT [14].

**7.2. Energy discrimination.** – The signal charge, produced in the HPD ( $U_C = 12$  kV), following the absorption of a 511 keV photon in a LSO crystals, ranges from 0.87 to  $1.23 \cdot 10^6$  electrons (0.14–0.2 pC), depending on the axial coordinate at which the crystal bar is hit. The induced signal on the back plane of the sensor is almost fully due to the holes drifting over the full thickness of the Si sensor (300  $\mu\text{m}$ ). The pathlength of the electrons (few  $\mu\text{m}$ ) does not give a sizable contribution. Operating the sensor above the full depletion voltage (“overbias”),  $U_{\text{bias}} \sim 3 \cdot U_{\text{dep}}$ , the  $\sim 10^6$  holes will induce a current of about 10  $\mu\text{A}$  during the total drift time of less than 15 ns. A low impedance and large bandwidth amplifier (70 MHz) with a shaping time of 5 ns will be able to sense about 1/3 of the total charge, *i.e.* about  $3 \cdot 10^5 e^-$ . Such an amplifier has a typical noise of about  $2 \cdot 10^3 e^-$  (RMS) even though the backplane capacitance is about 300 pF. This means that the back plane signal can be detected with a very comfortable signal to noise ratio of about 150.

The signal from the back plane of the silicon sensor is proportional to the total energy deposited in the crystal matrix. Therefore, it does not differentiate between a photoelectric interaction, where usually only one crystal bar is affected, and a detection sequence involving a Compton interaction, where generally several crystal bars are affected.

Summing just the analogue signals  $A_L$  and  $A_R$  of the left and right HPD does not provide an accurate energy discrimination. Due to the light absorption in the crystals, the sum  $A = A_L + A_R$  varies for the same energy deposit from 0.28 to 0.4 pC for interactions occurring at the centre and at the bar end, preventing the application of a precise cut for energy discrimination of  $S$  events. A threshold setting equivalent to 400 keV at the centre, for example, would correspond to a discrimination threshold of 310 keV at the bar end. By using instead the variable  $(A_L + A_R) - 0.5 \cdot |A_L - A_R|$  reduces the maximum dispersion by more than a factor two allowing a threshold of  $419 \pm 22$  keV.

A detailed description of the DAQ architecture which has been specifically designed for this project and its hardware implementation is given in [51].

## 8. – Conclusions

We described the innovative geometrical concept and a possible implementation of a 3D axial PET scanner and its dedicated data acquisition system. The performance estimates for the reconstruction resolution in both the axial and transaxial plane and the uniformity of the resolution over the complete field of view make the concept very competitive in comparison with existing state-of-the-art devices. The possibility to unambiguously reconstruct part of annihilation photons which underwent Compton scattering in the crystal matrix is a unique feature of the concept and leads to high sensitivity even for limited solid angle coverage. The use of recently developed fast high- $Z$  and high-density crystals like  $\text{LaBr}_3$  leads to excellent energy resolution, which is expected to facilitate scatter suppression and consequently will boost image contrast.

The described study is currently still on a conceptual level. Several findings require support by more elaborated and comprehensive simulations, which need to take into account effects linked to tomographic data reconstruction. A major milestone, the proof of principle in form of a 3D axial camera prototype module, is under preparation. Most of the required hardware components have been developed and are now available. We will report about the experimental results in a forthcoming paper.

\* \* \*

We would like to thank the numerous colleagues who helped in clarifying discussions to come to a better understanding of the potential and limitations of the proposed concept. Thanks to Wojtek Dulinski (LEPSI Strasbourg) for the mask design of the Silicon sensor. We acknowledge the great support of our technical personnel at CERN Francoise Cossey, Claude David, Luc Kottelat and Ian McGill, which was indispensable for the construction of the photodetector prototypes. We are grateful for the financial support by the CERN technology transfer service.

## REFERENCES

- [1] PHELPS M. E. and S. R. CHERRY, *Clin. Pos. Imag.*, **1** (1998) 31.
- [2] PHELPS M. E., *J. Nucl. Med.*, **41** (2000) 661.
- [3] MOSES W. W., *Nucl. Instrum. Methods A*, **471** (2001) 209.
- [4] SOSSI V., *Nucl. Instrum. Methods A*, **10** (2003) 107.
- [5] TALBOT J. N. *et al.*, *Nucl. Instrum. Methods A*, **504** (2003) 129.
- [6] PAVEL N. A., *Nucl. Instrum. Methods A*, **478** (2002) 1.
- [7] MARSDEN P. K., *Nucl. Instrum. Methods A*, **513** (2003) 1.
- [8] SOSSI V., *Resolution and sensitivity in positron emission tomography: New frontiers*, in *Proceedings of the 8th ICATPP Conference on Astroparticle, Particle, Space Physics, Detectors and Medical Applications*, edited by BARONA *et al.* (World Scientific) 2004, pp. 431-440.
- [9] KARP J. S. *et al.*, *J. Nucl. Med.*, **44** (2003) 1340.
- [10] WATANABE M. *et al.*, *IEEE Trans. Nucl. Sci.*, **49** (2002) 634.
- [11] SCHMANDT M. *et al.*, *IEEE Trans. Nucl. Sci.*, **45** (1998) 3000.
- [12] WIENHARD K. *et al.*, *IEEE Trans. Nucl. Sci.*, **49** (2002) 104.
- [13] ERIKSSON L., WIENHARD K., ERIKSSON M., CASEY M. E., KNOESS C. *et al.*, *IEEE Trans. Nucl. Sci.*, **49** (2002) 2085.
- [14] SCHMANDT M. *et al.*, *Performance evaluation of a new LSO High Resolution Research Tomograph HRRT*, in *Proceedings of IEEE Nuclear Science Symposium and Medical Imaging Conference, 1999 Seattle, WA*, pp. 1066-1071.
- [15] ZAIDI H., MONTANDON M.-L. and SLOSMAN D. O., *Med. Phys.*, **30** (2003) 937.

- [16] SHIMIZU K. *et al.*, *IEEE Trans. Nucl. Sci.*, **34** (1988) 717.
- [17] BRAEM A., CHAMIZO M. LLATAS, CHESI E. *et al.*, *Phys. Med. Biol.*, **49** (2004) 2547.
- [18] CHAMIZO M. LLATAS *et al.*, *High resolution 3D brain PET with hybrid photon detector*, in *Proceedings of the 8th ICATPP Conference on Astroparticle, Particle, Space Physics, Detectors and Medical Applications*, edited by BARONA M. *et al.* (World Scientific) 2004, pp. 391-394.
- [19] BRAEM A., CHAMIZO M. LLATAS, CHESI E. *et al.*, *Nucl. Instrum. Methods A*, **525** (2004) 268.
- [20] MELCHER C. L., *J. Nucl. Med.*, **41** (2000) 1051.
- [21] HELL E. *et al.*, *Nucl. Instrum. Methods A*, **454** (2000) 40.
- [22] C. W. E VAN ELJK, *Nucl. Instrum. Methods A*, **471** (2001) 244.
- [23] DORENBOS P., *Nucl. Instrum. Methods A*, **486** (2002) 208.
- [24] MOSES W. W., *Nucl. Instrum. Methods A*, **487** (2002) 123.
- [25] VAN ELJK C. W. E., *Nucl. Instrum. Methods A*, **509** (2003) 17.
- [26] SHAO Y. *et al.*, *IEEE Trans. Nucl.*, **49** (2002) 649.
- [27] SURTI G. *et al.*, *IEEE Trans. Nucl. Sci.*, **50** (2003) 348.
- [28] VAN LOEF E. V. D. *et al.*, *Nucl. Instrum. Methods A*, **486** (2002) 254.
- [29] VAN LOEF E. V. D. *et al.*, *Nucl. Instrum. Methods A*, **496** (2003) 138.
- [30] SHAH K. S., *Nucl. Instrum. Methods A*, **505** (2003) 76.
- [31] VILARDI I. *et al.*, to be published in *Nucl. Instrum. Methods A* (2006).
- [32] PETROSYAN A. G. *et al.*, *Nucl. Instrum. Methods A*, **486** (2002) 74 and references therein.
- [33] JORAM C., *Nucl. Phys. B (Proc. Suppl.)*, **78** (1999) 407.
- [34] D'AMBROSIO C. and LEUTZ H., *Nucl. Instrum. Methods A*, **501** (2003) 463.
- [35] JORAM C., *HPD and MAPMT-Segmented Photon Detectors for HEP and Beyond*, in *Proceedings of the workshop on Innovative Detectors For Supercolliders. 4-10 Oct. 2003, Erice, Sicily (Italy)*, edited by NAPPI E. and SEGUINOT J. (World Scientific) 2004.
- [36] MUSIENKO Y., *Advances in Avalanche Photodiodes, Proceedings of the Workshop on Innovative Detectors For Supercolliders. 4-10 Oct. 2003, Erice, Sicily (Italy)*, edited by NAPPI E. and SEGUINOT J. (World Scientific) 2004.
- [37] RENKER D., *Nucl. Instrum. Methods A*, **486** (2002) 164.
- [38] FARRELL R. *et al.*, *Nucl. Instrum. Meth. A*, **442** (2000) 171
- [39] SHAH K. S. *et al.*, *APD arrays for High Resolution PET*, *SPIE, 44th Annual Meeting, July 28-23, 1999*.
- [40] KAPUTSA M. *et al.*, *Nucl. Instrum. Methods A*, **504** (2003) 139.
- [41] EVRARD O. *et al.*, *Nucl. Instrum. Methods A*, **504** (2003) 188.
- [42] LECOMTE R. *et al.*, *Nucl. Instrum. Methods A*, **423** (1999) 92
- [43] MC INTYRE R. J., *IEEE trans. ED-13* (1972) 164.
- [44] JORAM C., *An Apparatus for the construction of Large Area Hybrid Photodiodes, Proceedings of the Workshop on New Detectors. 1-7 Nov. 1997, Erice, Sicily (Italy)*, edited by WILLIAMS C. and YPSILANTIS T. (World Scientific) 1998.
- [45] BRAEM A. *et al.*, *Nucl. Instrum. Methods A*, **442** (2000) 128.
- [46] BRAEM A. *et al.*, *Nucl. Instrum. Methods A*, **478** (2002) 400.
- [47] BRAEM A. *et al.*, *Nucl. Instrum. Methods A*, **502** (2003) 205.
- [48] BRAEM A. *et al.*, *Nucl. Instrum. Methods A*, **497** (2003) 202.
- [49] CHESI E. *et al.*, *A segmented Hybrid Photon Detector with integrated auto-triggering front-end electronics for a PET scanner*, to be published in *Nucl. Instrum. Methods A*.
- [50] DERENZO S. E., MOSES W. W., HUESMAN R. H. and BUDINGER T. F., *Critical instrumentation issues for 2 mm resolution, high sensitivity brain PET*, in *Quantification of Brain Function*, edited by UEMURA K., LASSEN N. A., JONES T. *et al.* (Elsevier Science Publishers, Amsterdam, The Netherlands) 1993, pp. 25-37, LBNL-34332.
- [51] DRAGONE A. *et al.*, *An Event Driven Read-out System for a Novel PET Scanner with Compton Enhanced 3D Gamma Reconstruction*, to be published in *IEEE Trans. Nucl. Sci.*, **53** (2006).